

PHOTON OPTICS AT SCSS

M. Yabashi^{1,2}, T. Hirono^{1,2}, H. Kimura^{1,2}, H. Ohashi¹, S. Goto¹, S. Takahashi^{1,2},
K. Tamasaku², and T. Ishikawa^{1,2}

¹ SPring-8/JASRI, Kouto 1-1-1, Sayo, Hyogo 671-5198, Japan

² SPring-8/RIKEN, Kouto 1-1-1, Sayo, Hyogo 671-5148, Japan.

Abstract

Vacuum ultraviolet (VUV) optics for the SCSS Prototype Accelerator (electron beam energy of $E_B = 250$ MeV) and X-ray optics for SCSS ($E_B = 8$ GeV) are summarized. The VUV optics have been designed for the diagnostics of the photon-beam properties in order to optimize the operation parameters of the accelerator. The system covers a radiation energy in the pulse from pJ to $\geq 10 \mu\text{J}$ in the visible to VUV range. The first results were obtained during the commissioning period in the spring of 2006. In the latter part, R&D for x-ray free-electron laser (XFEL) optics at SPring-8 are introduced. Qualities of crystals, mirrors, and windows have been improved for coherent x-ray applications.

VUV OPTICS FOR SCSS PROTOTYPE ACCELERATOR

Introduction

The SCSS Prototype Accelerator [1] has been constructed for investigating fundamental performance of the accelerator system, which has been originally designed for the Japanese XFEL project, SCSS [2]. The Prototype machine is composed of a thermionic electron gun [3], an injector system, a main accelerator system with C-band linacs, and a couple of undulators. The undulators (with a period of 15 mm, a total period number of 600, and a minimum gap of 3 mm) produce VUV radiation with a wavelength range shorter than 60 nm at an electron beam energy of 250 MeV. Strong SASE radiation is emitted with the optimized operation conditions.

The photon diagnostics system has been constructed for the single-shot measurement of photon-beam properties such as spectrum, radiation energy, spatial profile. These parameters are crucial for studying accelerator conditions and for tuning SASE amplification. The system covers a wavelength range from visible (including a wavelength of 633 nm for the alignment with a He-Ne laser) to VUV light (≥ 30 nm), and a radiation energy in the pulse from pJ (spontaneous radiation) to $\geq 10 \mu\text{J}$ (SASE saturated radiation).

The system has been designed in the beginning of 2005, and installed during the summer construction period. The first beam of the visible light was observed in the end of November. After the replacement of some optical components, the system has been dedicated for the VUV diagnostics in the commissioning period from May to July of 2006. In particular, the first lasing was observed in June,

15th. After the first lasing, the beam tuning has been proceeded for optimizing SASE condition.

Design and Evaluation

General The schematic of the system is shown in Fig. 1. The components are placed on two granite tables, which are common designs to those used in the accelerator section. The beam pipes and components are evacuated with turbo-molecular pumps to a vacuum level of $\leq 10^{-6}$ Pa. Since the average power of the incident radiation is smaller than 1 mW at a maximum, cooling for optical components is unnecessary. A plane mirror (Au coating on a SiO_2 substrate for VUV; Al coating on a SiO_2 substrate for visible light) with a deflection angle of 170° is placed at the downstream of the first table for eliminating high-energy bremsstrahlung. A dispersive spectrometer, which is composed of an incident slit, a concave grating, and a charge-coupled device (CCD), is located in the second table. Several pneumatic actuators (indicated as monitors in Fig. 1) are prepared for inserting detectors, screens, and optical components in the beam path. At the upstream of the first table, a CCD camera and a movable plane mirror are installed for monitoring the He-Ne laser, which is used both for the alignment of the upstream components in the accelerator section and for this optical system.

Spectrometer The spectrometer is designed in a normal-incidence, constant-deviation geometry. The radius of the concave grating, the deflection angle, and the distance between the incident slit and the grating are $R = 922$ mm, $\gamma = 25^\circ$, and $L_i = 1615$ mm, respectively. The wavelength λ focused in the center of the CCD is controlled by changing the incident angle of the grating, α , and the distance between the grating and the CCD, L_o , so as to satisfy the following equations simultaneously,

$$\frac{\cos^2 \alpha}{L_i^2} + \frac{\cos^2 (\alpha - \gamma)}{L_o^2} = \frac{\cos \alpha + \cos (\alpha - \gamma)}{R}, \quad (1)$$

and

$$\sin \alpha + \sin (\alpha - \gamma) = mN\lambda, \quad (2)$$

where m and N are the diffraction order and the line density of the grating, respectively. Two laminar gratings (Shimadzu Corp., Al coating with 600 lines/mm; Au coating with 2400 lines/mm) are prepared for covering longer (≥ 100 nm) and shorter (≤ 200 nm) wavelength region, respectively.

In the dispersed beam from the grating, different wavelengths are focused at different horizontal positions on the

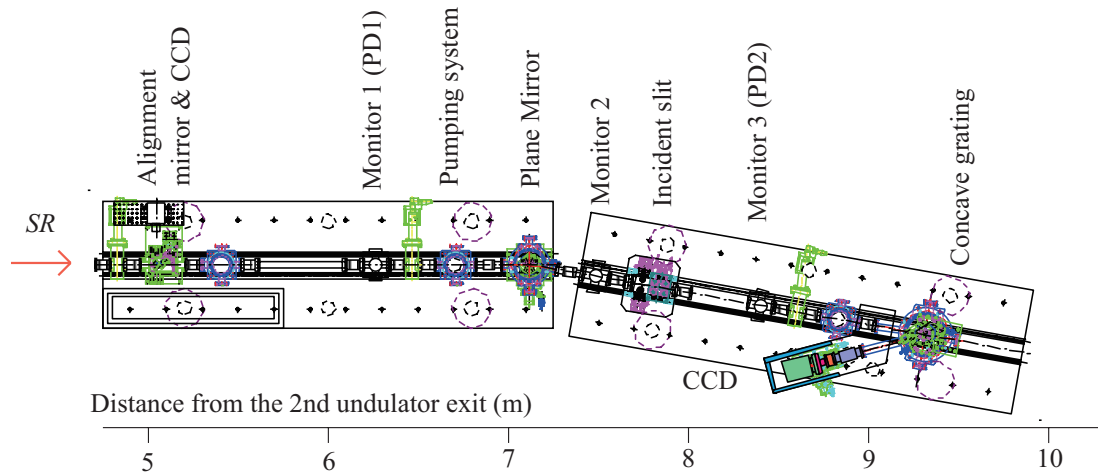


Figure 1: Layout of the optical system.

CCD. (Princeton Instruments Inc., PI-SX 400-1340B). The device, which has a back-illuminated sensor with electric cooling, covers from visible to the x-ray range. A pixel number and a pixel size are $1340 (h) \times 400 (v)$ and $20 \times 20 \mu\text{m}^2$, respectively. In the vertical direction, the concave grating simply works as a concave mirror. Thus, the vertical intensity distribution corresponds to a real image in the vicinity of the incident slit. An example of the spectrum image measured with the He lamp is shown in Fig. 2 (a).

The spectrum resolution is determined mainly from the following conditions: i) the line number in the illuminated area of the grating; ii) the spatial resolution of CCD; and iii) the aberration. Note that the incident beam to the slit is the quasi-plane wave, not focused as usual, because the plane mirror is used as a pre-optic. Thus the illuminated area on the grating is determined mainly by the beam divergence of the plane-wave diffraction at the slit.

Figure 3 shows calculated resolutions at a slit width of $100 \mu\text{m}$ and a detector resolution of $60 \mu\text{m}$ (3 pixels). The measured values using a helium lamp (He I, $\lambda = 58.43 \text{ nm}$) and a mercury lamp (Hg I, $\lambda = 184.95$ and 253.65 nm) at the same slit width are also indicated in the figure. The measured results are mostly agreed with that calculated with the detector limitation. The resolution $\lambda/\Delta\lambda$ is greater than 1000 even at $\lambda = 58.4 \text{ nm}$ [see Fig. 2 (b)]. We note that a ray-trace calculation shows that the effect of the aberration is smaller than the other two factors. This result is supported by the experiment.

The spectrometer can be used for measuring a spatial profile at the slit position by switching the diffraction condition to the 0th order.

Intensity monitor Single-shot radiation intensities are measured with photodiodes, which are installed in the front of the mirror (PD1) and in the downstream of the slit (PD2). They are inserted to the beam axis by the remote control. The devices are designed for high-dose measurement (IRD Inc., SXUV100; SXUV100RPD [4]) with sensor sizes of

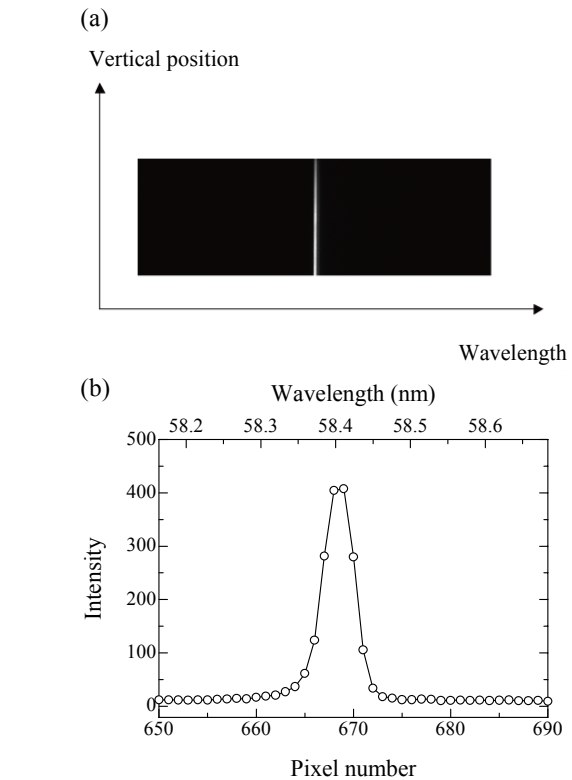


Figure 2: (a) Spectrum image measured with He lamp. The horizontal axis is the dispersive direction, where the right direction corresponds to longer wavelength. The vertical axis corresponds to the real image in the vicinity of the incident slit. (b) Intensity distribution along horizontal pixels, after the average over vertical pixels of (a). The upper axis shows the corresponding wavelength.

$10 \times 10 \text{ mm}^2$. The sensors are combined with a charge amplifier (PA-100) or with an oscilloscope. The gain of amplifier can be changed by a factor of 10^5 . The signal is connected into the accelerator control system using an A/D

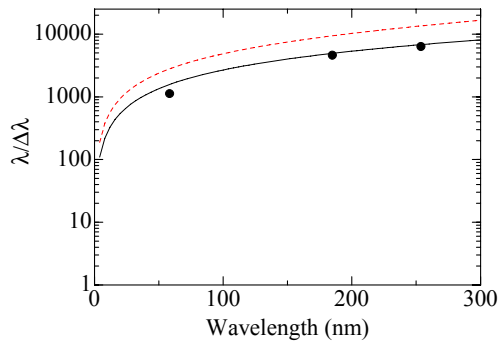


Figure 3: Resolution of spectrometer with a line density of grating of 2400 lines/mm. The dashed and solid lines are calculated results from the line number and the detector resolution, respectively. The solid circles are measured values.

converter.

Commissioning results

Spectrum Spectrum measurements for spontaneous and SASE radiations have been dedicated for tuning and evaluating the following conditions: i) optimization of electron-beam conditions including orbit, focusing, bunching condition, etc.; ii) tuning of undulators; iii) evaluation of the electron-beam density from SASE spectrum. In particular, the last [1].

The spectrum data are obtained typically with 100-shots accumulation for spontaneous light, and with single shot for SASE radiation. Figure 4 (a) shows a single-shot spectrum for SASE radiation at an electron charge of 0.24 nC, an undulator gap of 3 mm, and a slit width of 100 μm . The arc shape of the spectrum indicates that the wavelength tends to longer in the peripheral area, which is a similar phenomenon to the spontaneous radiation. The split into several lines are due to the fact that the beam is multimode. Figure 4 (b) shows a central, on-axis spectrum. The central wavelength is determined to be $\lambda = 59.0 \text{ nm}$ with a FWHM of $\Delta\lambda = 0.234 \text{ nm}$.

The pulse length can be estimated from the spectrum. For example, if one assume that the pulse has a rectangular shape, the energy bandwidth ΔE and the pulse width Δt is represented as,

$$\Delta E \cdot \Delta t = 3.6 \text{ (eV} \cdot \text{fs)}, \quad (3)$$

in the Fourier-limited pulse. In our case, $\Delta E = 0.083 \text{ eV}$ is simply deduced from the relationship $\Delta E/E = \Delta\lambda/\lambda$. Then the pulse width is estimated to be $\Delta t = 43 \text{ fs}$.

Radiation intensity The radiation intensities measured with photodiodes are particularly used for quick optimization of the operation parameters such as electron-beam orbit, bunching condition, timing, beam collimation, alignment of undulators, etc.

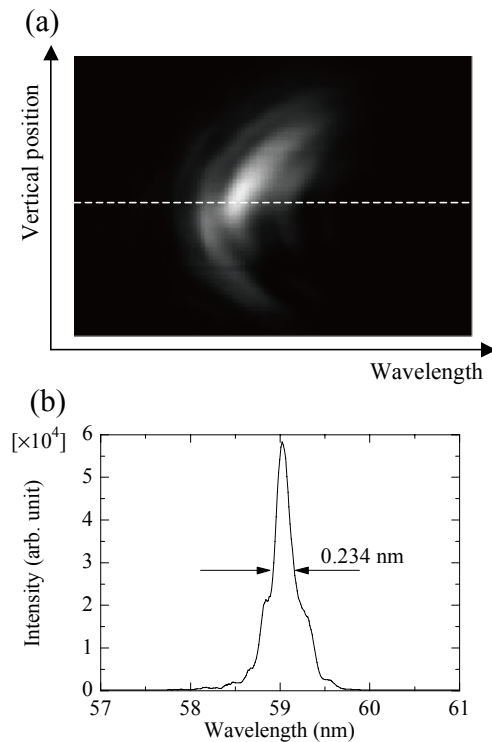


Figure 4: (a) Single-shot image of SASE radiation. (b) On-axis spectrum of (a) along the dashed line.

The conversion from the output charge to the absolute intensity is necessary for evaluating SASE energy. At present, we use a catalog table [4] for referring the efficiency (*i.e.*, output charge of the detector per incident energy of the radiation pulse). However, it is desirable to determine the efficiency experimentally. For the purpose, we have tested a calibration method using the spontaneous radiation. First, the accelerator parameter is set to be debunching condition for producing only spontaneous radiation. Then the output charge per pulse is measured. The theoretical radiation energy to the detector is calculated using the sensor size and the distance to the detector. This partial energy has small dependences of machine parameters except the electron-beam energy and the charge. Thus the efficiency can be accurately obtained from the normalization of the measured charge by the calculated partial energy. The important point of the method is to choose moderate K parameter; the contamination of higher-order radiation is increased at a large K , while the dependence of the energy on K is too large at a small value. The optimized value is considered to be 0.2 to 0.7.

Figure 5 shows efficiencies of PD1 and PD2, measured with changing K parameter of the first undulator from 0.2 to 0.73. The catalog values are also indicated. The efficiency of PD1 is agreed with the catalog value within a 30 % deviation. Smaller values in PD2 are explained by the fact that PD2 is located in the downstream of the Au mirror, which has a reflectivity of $\sim 80 \%$. Thus, it is plausible that the method can be applied to the quick check of

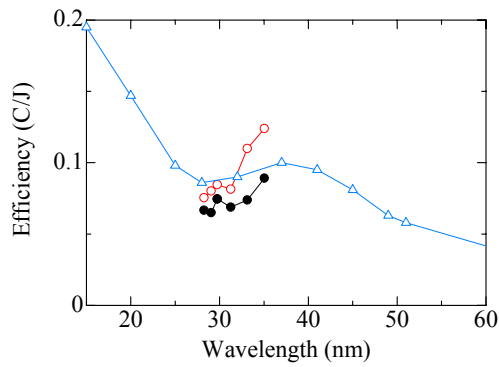


Figure 5: Detector efficiencies for PD1 (red open circles) and for PD2 (black closed circles). The blue open triangles show the catalog values.

the efficiency. We are planning to install thin-metal attenuators, because the present maximum energy, around $2 \mu\text{J}$, is nearly the saturation level of the detector. The above calibration method is effective even in this case. We note that the efficiencies in a wavelength range longer than 35 nm will be measured with low-energy operation of the accelerator.

Spatial profile and coherence The spatial profile at the slit position is measured using the 0th-order diffraction of the grating, where the grating simply works as a spherical mirror. Figure 6 (a) shows a single-shot image at a lasing condition only using the first undulator. The horizontal (vertical) width and divergence (in FWHMs) are determined to be 3.4 (3.9) mm and 240 (280) μrad , respectively, using a distance of 13.9 m from the undulator exit to the slit, as seen in Fig. 6 (b).

The spatial coherence is evaluated with a Young's double-slit experiment. The double slit with each width of $100 \mu\text{m}$ (height of $500 \mu\text{m}$) and a central spacing of $400 \mu\text{m}$ were installed at the incident slit position. The grating was replaced with a plane mirror, and the diffraction image was recorded with the CCD, as shown in Fig. 7. The image with SASE radiation (single-shot detection) is compared to that at spontaneous radiation (100 shots). The former image has a higher visibility [Fig. 7 (c)], which indicate higher spatial coherence. We are planning to make more quantitative measurement using double slits with different spacings.

Extension for user experiment

In 2007, we are planning to start the operation dedicated for user experiments. A present plan for the extension is as follows: The experimental hall (about $12 \times 8 \text{ m}^2$) is constructed at the outside of the accelerator tunnel. The beam transport channel is branched from the middle of the present diagnostic system. The beam is two-dimensionally collimated with double mirrors. A gas chamber with a differential pumping system is installed for a transparent, shot-by-shot monitor for the radiation intensity.

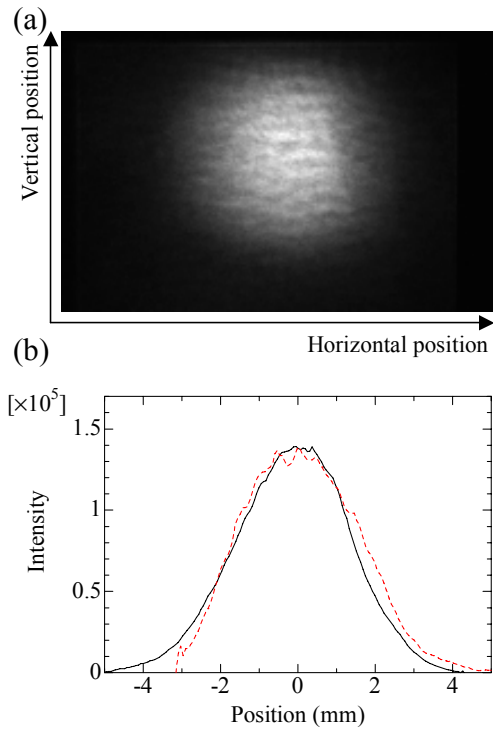


Figure 6: Spatial profile of SASE radiation (a), and its projections for horizontal (solid line) and the vertical (dashed line) axes (b).

X-RAY OPTICS FOR SCSS

Introduction

The principal missions of the optics in XFEL are i) to condition photon beam for user experiments, and ii) to diagnose radiation properties for the feedback to the accelerator. In this section, we will introduce R&D activities proceeded at SPring-8.

There are two technological challenges in XFEL optics. One is to suppress speckles possibly originating from imperfections of optical components under the coherent illumination. Both surface and bulk qualities should be strictly controlled.

The other is to keep the radiation dose below the melting limit [5, 6]. A simple solution is to extend the x-ray transport line for decreasing the energy density. However, in the SCSS case, the magnification of the beam area, when compared to that at the entrance of the beamline, is not larger than 10 because of small beam divergence ($0.4 \mu\text{rad}$ at $E=12.4 \text{ keV}$, for example) and the limited distance of $\sim 200 \text{ m}$. An alternative method is to use components made from light elements such as Be, B, C, etc. Figure 8 shows calculated doses for several materials that are placed normal to the incidence. The following beam parameters [2] are used for the calculation: the photon flux of 7.6×10^{11} photons/pls, the STD beam size at the source of $50 \mu\text{m}\phi$, and the distance from the undulator exit of 100 m. The STD beam divergence is calculated from the diffrac-

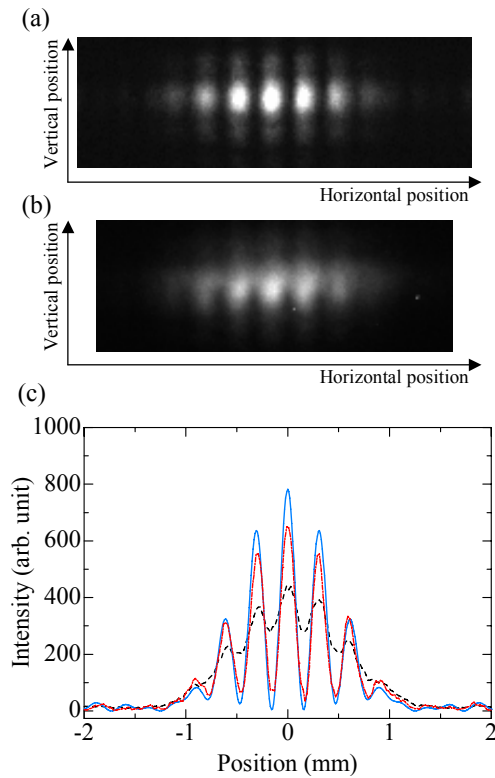


Figure 7: Young's double-slit experiment for SASE radiation with single shot (a), and for spontaneous radiation with 100 shots (b). The cross sections of the central region at these conditions are shown in (c) as the red dot-dashed and black dashed line, respectively. A calculated result under the coherent illumination is also represented as a blue solid line.

tion limited condition for each photon energy. It is found that i) the doses of light materials (Be and C) have a margin to the threshold levels more than two-order of the magnitude, and ii) the dose of Si is still below the threshold, but iii) the dose of Cu is above threshold in the energy range higher than the K-absorption edge.

Crystals and windows

Crystal monochromator is used to set specific spectral window at SASE and spontaneous radiation. We have two candidates for crystal materials: Si and diamond. The energy resolutions ($\Delta E/E$) are 1×10^{-4} and 6×10^{-5} for Si (111) and Diamond (111) reflections, respectively.

Si is the most popular materials for monochromator crystal at the present synchrotron facilities, because of the availability of high-quality, large-volume ingots. Since the Bragg angle for (111) reflection at $E = 10$ keV is 11 degree, the dose per atom around this photon energy is decreased by a factor of 5, compared to the normal incidence case shown in Fig. 8. The ratio is further increased for higher photon energy (*i.e.*, lower Bragg angle). Thus, Si would be useful as XFEL monochromator above 10 keV. Crystal cooling is not a serious problem for SCSS. Because

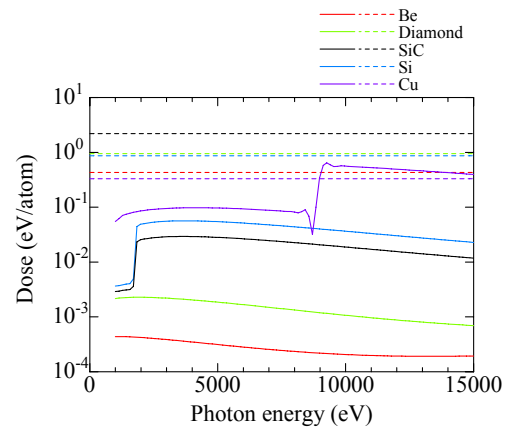


Figure 8: Energy dependence of dose for several materials. Solid lines are calculated values with SCSS beam parameters, while dashed lines are the threshold levels of melting limit.

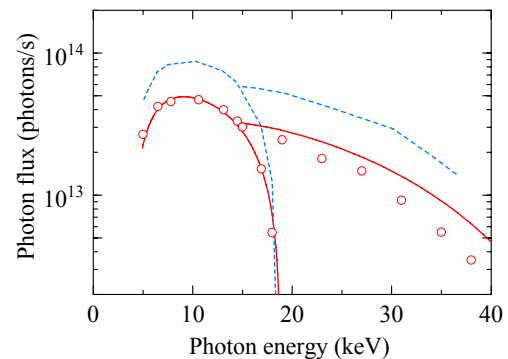


Figure 9: Photon flux of the monochromatic beam at SPring-8 undulator beamlines. The open circles and solid lines are measured and calculated values for diamond monochromator, respectively, and the dashed lines are measured values for cryogenically-cooled Si monochromator.

the average power is smaller than 100 mW, water cooling would be sufficient.

Diamond monochromator is the most promising when utilized under a higher dose. We have collaborated with Sumitomo Electric Industries Ltd. (SEI) to develop high-quality synthetic diamond in type IIa [7]. Recently, (111) crystal plates with relatively large sizes ($\sim 8 \times 4$ mm²) are commercially available. We have tested performance of diamond double-crystal monochromator (DCM) at a SPring-8 undulator beamline. Two (111) diamonds crystals, which are attached to copper crystal holders using indium sheets, are cooled by water. Figure 9 shows the measured photon flux. Experimental results are well agreed with the theory in the energy range below 20 keV. Topographic studies showed a relationship between the surface condition and the image quality. It is necessary to develop surface polishing technique.

For windows, Be foils have been widely used at syn-

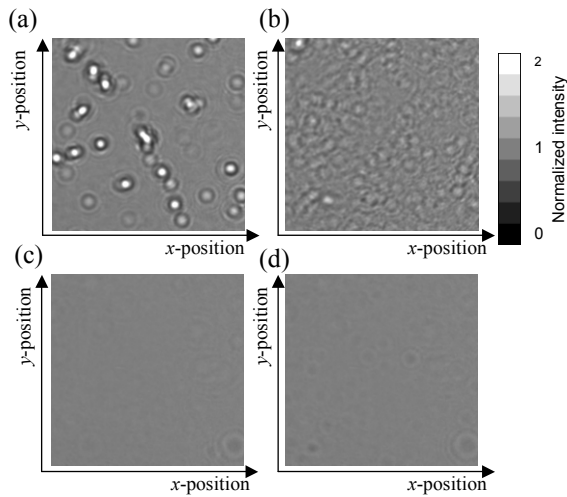


Figure 10: Transmission images of Be windows: Polished PF-60 (a), polished IF-1 (b), polished PVD (c), and Kapton foil (d). The photon energy is $E = 12.4$ keV. The beam areas are $300 \times 300 \mu\text{m}^2$. The distance between the sample to the camera is 1400 mm. The round spots commonly seen at the bottom-right corners of (c) and (d) are caused from a Kapton foil in the upstream of the system.

chrotron facilities owing to their low absorptions for x-rays. They are also promising candidates for XFEL windows from the viewpoint of the dose issue (see Fig. 8). However, it has been found that they produced speckles under coherent illumination. From the experiment at the 1 km beamline of SPring-8, it was found that the speckles in the conventional Be windows shown in Fig. 10 (a,b) are originated mainly from voids in the bulk [9]. To remove the voids, the physical vapor deposition (PVD) method has been tested. The surface of the PVD Be foil has been polished to decrease the surface roughness to be $0.05 \mu\text{m}$. Finally, the image of a polished PVD Be shown in Fig. 10 (c) was found to be superior to that of a Kapton foil in (d) [10]. We note that Be will be useful for attenuators. Higher attenuation will be achieved using Si or SiC.

Mirror

Total-reflection mirrors are used for deflecting SASE radiation in order to eliminate high-energy bremsstrahlung. Focusing is another important function of the mirror. The surface quality is crucial for suppressing speckles under coherent illumination. From 2000, we have collaborated with Osaka University to realize high-quality mirrors. Special techniques of surface polishing have been developed: EEM (Elastic Emission Machining) and PCVM (Plasma Chemical Vaporization Machining) [11]. Figure 11 shows reflected images of Si mirrors measured at the 1 km beamline with a photon energy of $E = 20$ keV. The incident angles and the distance between the mirrors to the camera are set at 1.2 mrad and 966 mm, respectively. The intensity fluctuations observed with the pre-machined surface in

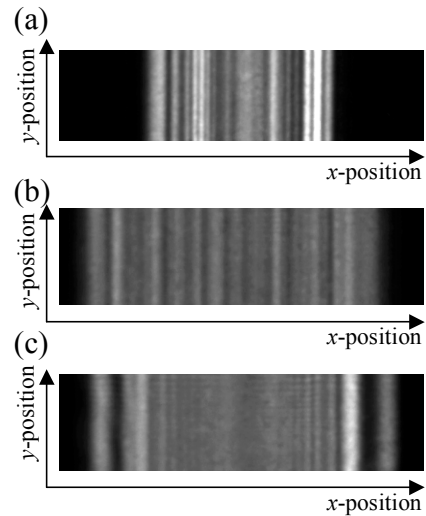


Figure 11: Reflection images of Si mirrors: Pre-machined surface (a), PCVM polished surface (b), and PCVM+EEM polished surface (c).

Fig. 11 (a) are mostly suppressed with the PCVM+EEM polished mirror in (c). Thus, we can conclude that the mirror is available for conditioning coherent x-rays.

These machining techniques with combination of a new metrological method called the microstitching interferometry (MSI) [12] were applied to fabrication of aspherical mirrors for nano-focusing. A couple of Pt-coated mirrors are fabricated with figure accuracies of 2 nm (p-v). Two dimensional focusing down to $36 \times 48 \text{ nm}^2$ has been achieved at $E = 15$ keV with the Kirkpatrick-Baez arrangement [13].

Another critical issue for the XFEL mirror is to choose appropriate surface material to suppress the dose under the melting limit [5]. Figure 12 shows the calculated doses and reflectivities for several materials. The beam parameters are as same as those used in Fig. 8 with a photon energy of $E = 12.4$ keV. It is found that C or SiC seems to be useful, while Si and Au are questionable. From the figure, the incident angles should be smaller than 2 mrad (0.14 degree). If we set an acceptance width to be 1 mm, the total length of the mirror should be larger than 500 mm. Thus, the next R&D issues for XFEL mirror fabrication are i) to study coating and polishing method for the light materials, and ii) to product large mirror with a sufficient figure accuracy. It is also important to establish technologies to protect the surface from contaminations or dusts, because small decrease of reflectivity can cause serious damage of the surface under the high-dose irradiation. Great care should be required in the design of the driving mechanism in order to keep an ultraclean environment.

Single-shot spectrometer

As shown in the previous section, the VUV single-shot spectrometer has played a central role for the radiation diagnostics. Development of similar instrument that works

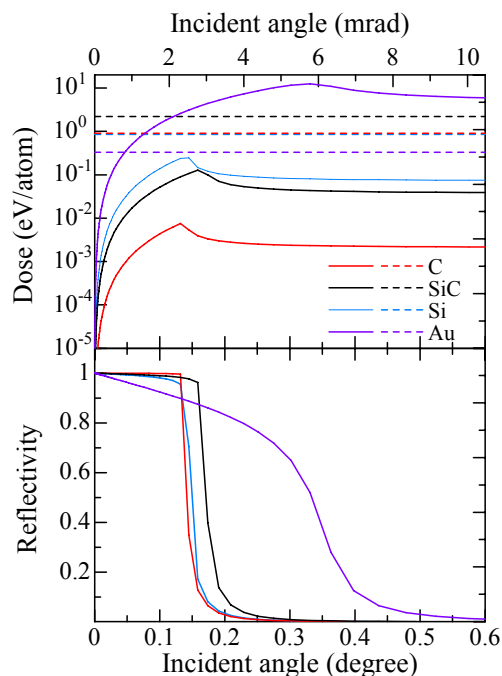


Figure 12: (above) Angular dependences of doses for the total reflection mirrors. Several materials are compared. Solid lines are calculated values with SCSS beam parameters, while dashed lines are the threshold levels of the melting limit. (below) Dependences of reflectivities.

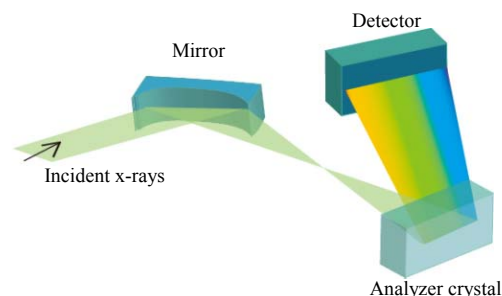


Figure 13: Setup for single-shot x-ray spectrometer.

in the x-ray region is crucial. Recently, we have developed such a spectrometer that combines a high-quality mirror and a Si flat crystal. The former is used to diverge the incident parallel beam, while the latter is to select specific energy according to the Bragg's law. As a result, the exit beam has an energy dispersion. The key point is again the figure accuracy of the mirror to suppress speckles. Using (555) reflection for the analyzer crystal, the energy resolution of the instrument has been measured to be 13.1 ± 1.9 meV at $E = 10$ keV with a full energy range of ~ 3 eV. Wider energy range can be easily obtained by changing diffraction plane to lower index [14].

SUMMARY

The VUV diagnostic system for the SCSS prototype accelerator has been constructed and successfully operated. At a lasing condition, a radiation energy in the pulse has been evaluated to be $\sim 2 \mu\text{J}$. The pulse width is estimated to be shorter than 100 fs from the measurement of the energy spectrum. The double-slit experiment showed that higher spatial coherence is achieved at a lasing condition.

As XFEL optical components, we have developed high-quality diamonds, mirrors, and Be windows. A single-shot spectrometer for XFEL diagnostics has been tested and confirmed to have a high resolution of 1.3×10^{-6} at $E = 10$ keV.

ACKNOWLEDGEMENT

We thank all SCSS members for fruitful discussions and suggestions. We acknowledge Dr. Y. Takata (RIKEN), Dr. Y. Harada (RIKEN), and Dr. T. Tokushima (RIKEN) for their suggestions on designing the spectrometer, Dr. A. Higashiya (RIKEN), Dr. T. Matsushita (JASRI), Dr. Y. Tamenori (JASRI), and Dr. A. Sekiyama (Osaka Univ.) for their help in the calibration of the spectrometer, Mr. T. Kirimura (RIKEN) for the calibration of the photodiodes, Mr. M. Tanaka (JASRI), Mr. T. Irie (JASRI), and Mr. K. Onoe (ULVAC) for their activities in the installation of the VUV diagnostic system.

REFERENCES

- [1] H. Tanaka et al., in these proceedings.
- [2] "SCSS X-FEL Conceptual Design Report", RIKEN/SPring-8, May 2005, Mikazuki, Japan, <http://www.xfel.spring8.or.jp/>
- [3] K. Togawa et al., "Emittance Measurement on the CeB₆ Electron Gun for the SPring-8 Compact SASE Source", FEL 2004 conf. proc. (2004) THBOC03.
- [4] International Radiation Detector Inc., <http://www.ird-inc.com/>
- [5] R. Tatchyn, "LCLS Optics: Technological Issues and Scientific Opportunities", SLAC-PUB-6064, SLAC, Stanford (1993).
- [6] "Linac Coherent Light Source (LCLS) Conceptual Design Report", SLAC-R-593, SLAC, Stanford (2002).
- [7] K. Tamasaku, T. Ueda, D. Miwa, and T. Ishikawa, "Goniometric and topographic characterization of synthetic Ila diamonds", J. Phys. D: Appl. Phys. **38** (2005) A61.
- [8] M. Yabashi et al., "Diamond double-crystal monochromator for SPring-8 undulator beamlines", Proc. for SRI 2006 (in press).
- [9] S. Goto, M. Yabashi, K. Tamasaku, S. Takahashi, and T. Ishikawa, "Characterization of Beryllium Windows using Coherent X-rays at 1-km Beamline", AIP conf. proc. **705** (2004) 405.
- [10] S. Goto, M. Yabashi, K. Tamasaku, and T. Ishikawa, "Characterization of Beryllium Windows for Coherent X-ray Optics", Proc. for SRI 2006 (in press).

- [11] Y. Mori et al., "Development of plasma chemical vaporization machining and elastic emission machining systems for coherent X-ray optics", Proc. SPIE, Vol. 4501 (2001) 30.
- [12] K. Yamauchi et al., "Microstitching interferometry for x-ray reflective optics", Rev. Sci. Instrum. **74** (2003) 2894.
- [13] H. Mimura et al., "Hard X-ray Diffraction-Limited Nanofocusing with Kirkpatrick-Baes Mirrors", Jpn. J. Appl. Phys., **44** (2005) L539.
- [14] M. Yabashi et al., "Single-shot spectrometry for x-ray free-electron laser", Phys. Rev. Lett. **97** (2006) 084802.

X-RAY DETECTORS AT DESY

H. Graafsma, DESY, Hamburg

Abstract

The European X-ray Free Electron Laser to be constructed in Hamburg, presents interesting challenges for the X-ray detectors. Every pulse of the XFEL represents an entire experiment of its own, partly because of sample degradation or destruction, and partly because of pulse to pulse fluctuations. Therefore, a maximum amount of data has to be collected in a single shot. This means first of all that photon counting detectors cannot be used, instead one has to construct integrating detectors, still with single photon sensitivity. Secondly, since the strength of the European XFEL is a very flexible pulse structure with high repetition rates, fast framing times down to 200 ns (5 MHz) are required. I will present some of the requirements imposed by the science cases foreseen at the European XFEL, and some of the possible solutions under consideration, both at DESY and at other places in the world.

**PAPER NOT
AVAILABLE**

WAVE-FRONT OBSERVATIONS AT FLASH

M. Kuhlmann, E. Plönjes, K. Tiedtke, S. Toleikis, HASYLAB at DESY, 22607 Hamburg, Germany
 P. Zeitoun, J. Gautier, T. Lefrou, D. Douillet, ENSTA, 91761 Palaiseau cedex, France
 P. Mercère, Synchrotron SOLEIL, 91192 Gif-sur-Yvette Cedex, France
 G. Dovillaire, X. Levecq, S. Bucourt, Imagine Optic, 91400 Orsay, France
 M. Fajardo, Centro de Física dos Plasmas, Instituto Superior Técnico, 1049-001 Lisboa, Portugal.

Abstract

During the first year of user operation at the Free-Electron Laser in Hamburg (FLASH) wave-front measurements were recorded in the vacuum-ultraviolet region using a Hartmann sensor (by Imagine Optic). The Hartmann principle is based on a hole array, which divides the incoming beam into a large number of sub-rays monitored in intensity and position of individual spots. The identification of the local slope of the incident wave front makes the aberrations from a perfect spherical wave front visible. Ray tracing in upstream direction accesses the beam path especially the focal spot in size and position.

The intense and coherent vacuum-ultraviolet FEL beam leads to unique requirements for the wave-front sensor setup. We report an optimized setup to observe the metrology of flat and curved mirrors at FLASH beam lines. The use of wave-front measurements to provide reliable machine parameter is discussed.

The wave-front sensor proved to be a valuable tool to observe the FEL beam quality and the performance of optical elements, filters and diagnostic tools.

GENERAL

FEL beam characteristics

The here-introduced wave-front sensor is used as tool in the photon diagnostics at FLASH. A free electron laser beam shows specific characteristics which demand certain requirements for any diagnostic tool.

Based on the SASE principle all FEL features differ from shot to shot depending on the degree of saturation. At a high level of some μJ per pulse the FEL operates in an intensity regime of two orders of magnitude. The required adaptations in the wave-front sensor setup and the needed data statistics which can document the shot to shot changes are discussed in the following sections.

The wavelength regime of 13 nm to 60 nm is of no consequence for the achromatically wave-front sensor. The short pulse length of 10 – 50 fs and the variable rates of repetition will be a challenge if the wave-front sensor becomes an online diagnostic tool in the future.

Wave-front measurements

In the regime of visible light sensors based on the Hartmann respectively the Shack-Hartmann principle are of common use. Astigmatism, spherical aberration and coma are quantitatively determined. Aberrations of such kind are generally of lower amplitude in the extreme-

ultra-violet or soft x-ray domain. For the first time Le Pape et al. used a wave-front sensor in the EUV regime. The experiment took place at a tabletop saturated soft-x-ray laser [1]. Here, the wave-front sensor shall be evaluated for

- FLASH beam line commissioning
- FEL characterisation
- Online diagnostics as part of user experiments

SETUP

Setup of the beam lines

Five beam lines are in operation mode for user experiments. At each an additional optical laser for pump-probe experiments is available. Figure 1 shows a scheme of the FLASH experimental hall. The beam lines discussed in the following are identified by the full-width-half-maximum (fwhm) beam size of their focal spot, considering the theoretical design parameters of the FEL. More than 10 switching or focusing mirrors are in use. Only one beam line can make use of the FEL beam at a time.

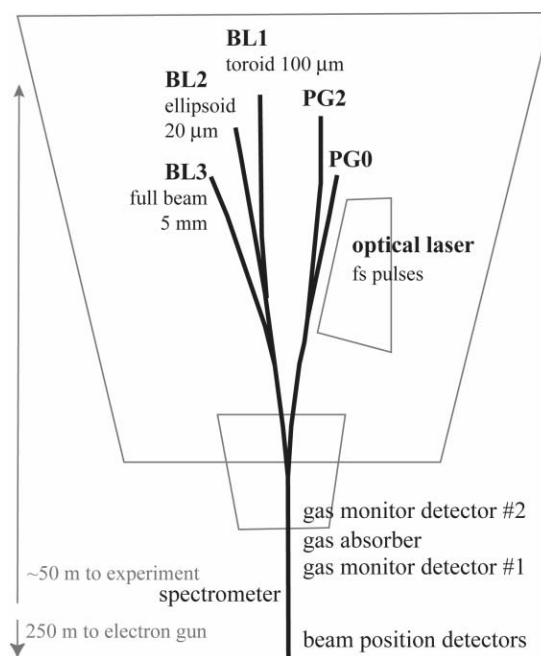


Figure 1: Scheme of the FLASH experimental hall and its beam lines. Some photon diagnostics tools are outlined along the FEL beam.

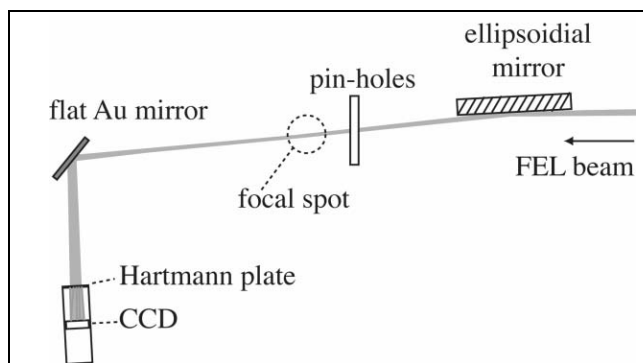


Figure 2: Setup for wave-front measurements at beam line BL2. The sensor is positioned 3.5 m behind the focal spot.

Up to now, the wave-front sensor was used at the beam lines BL1, 2, and 3. All are high intensity beam lines without a monochromator. Whereas at BL3 the unfocused FEL beam can be measured, BL1 and BL2 are designed to a focal spot size of approximately 100 μm and 20 μm , respectively. All switching and focusing mirrors working with an incident angle of 2 or 3 degree and have a carbon coating.

Setup of the wave-front sensor

A perfect spherical wave is compared with the actual beam to analyze its wave front. Therefore, both beams have to pass through a two dimensional array of holes (Hartmann plate) and are recorded under similar conditions on a CCD. Here, the Hartmann plate is made of nickel. It consists of 51 x 51 square holes each 110 μm in size and with a pitch of 387 μm . Therefore, the maximal field of view is 19.5 mm x 19.5 mm. The quadratic holes are tilted by 25° to prevent the long-range diffracted signal coming from one hole to interfere with the spot of the adjacent hole, generating an unpredictable error on data treatment. The sensor includes a direct CCD camera, PI-SX1300, with 1340 x 1300 pixels, each 20 μm in size. It is operated at -40° to minimize the noise level. In general, a zonal reconstruction is used to take as much pixels as possible into account [2]. To distinguish the contributions of higher order aberrations a modal reconstruction algorithm can be used, too. Imagine Optic provides the complete sensor.

Figure 2 is the sketch of a typical setup. The plotted example was build up at beam line BL2. The sensor is positioned in 3.5 m distance from the focal spot, more than the 2 m focal distance of the focusing ellipsoidal mirror. This allows for a full illumination of the sensor. A flat gold mirror placed in 45 degree absorbs 97% of the beam intensity at a wavelength of 32 nm. Currently, mirrors with gold, silver, and aluminium surfaces are used. The different mirrors are required to operate the sensor at different wavelengths and levels of intensity. Otherwise the camera pixels are generally saturated. Pinholes, generating a perfect spherical wave, can be moved in the beam to allow relative measurements. The sensor was calibrated using this setup in the direct beam without the additional mirror. Only than the FEL intensity

was sufficient to illuminate the full field of view of the sensor. A pinhole 5 μm in diameter was used.

BEAM LINE COMMISSIONING

The spatial characterization of the wave front has important applications in discovering localized defects in beam line optics. The proposed intensities of FLASH forced the beam line design to work with grazing incidences of 2° to 4° for both switching and focusing mirrors. The FEL wavelength of 60 nm to 13.1 nm in the fundamental demands full vacuum and particle free equipment towards the experiment. The task is to prove the feasibility of the sensor for the use as commissioning tool at FLASH.

Documentation of the focal spot size

Beam line BL2 consists of two flat switching mirrors and one focusing ellipsoidal mirror. The design proposed a spot size of 20 μm at a focal distance of 2 m. Figure 3 shows the depth of focus reconstructed from wave-front measurements in October 05. Displayed are the full-width-half-maximum (fwhm) values of the beam size at distinguished positions relative to the calculated focal point. The focal spot is reconstructed to a fwhm-size of 31 μm x 31 μm , an error of $\pm 2 \mu\text{m}$ is given by the Gaussian fit of the reconstructed beam spot. A minor astigmatism can be seen in Figure 3 according the difference in horizontal and vertical minimal focal spot position. With further investigations this problem was imputed to a switching mirror and was eliminated by remounting the mirror.

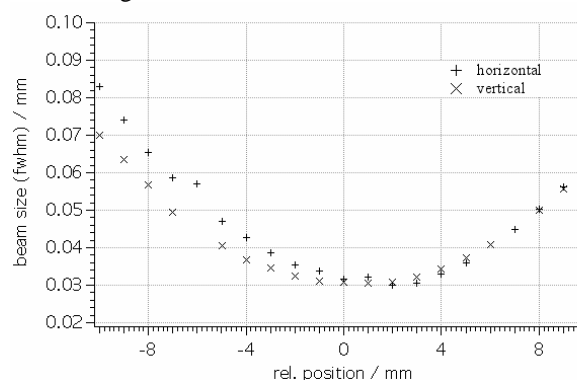


Figure 3: The depth of focus at beam line BL2 at a wavelength of 32 nm. Shown are fwhm values at distinguished distances from the measured focal position in vertical and horizontal direction. The minimal beam size is 31 μm x 31 μm ($\pm 2 \mu\text{m}$).

Nevertheless, the overall wave front here displayed in Figure 4 is of high quality. Displayed are absolute values of the difference to a perfect wave for each pixel. So the comparison of variable wavelengths of the FEL is possible. For wave-front analysis the generally used scaling in parts of lambda complicates the comparison and documentation of different measurements. The wave front can be characterized by the root-mean-square error rms=3nm and the peak-valley difference PV=19nm. The

wave front used for the calibration of the sensor was measured with $\text{rms}=0.64\text{nm}$ and $\text{PV}=4\text{nm}$. Additionally the position of the focal spot is recorded to allow for the shot to shot characteristic of the FEL. In the here shown early phase of the FEL operation an unstable beam correspond to a standard deviation of $4.5\ \mu\text{m}$ in spot size.

The design values for the beam line parameters are not achieved up to now. The wave-front measurements verify that the situation is not origin in a misalignment or in manufacturing errors of the optics. Further measurements at the unfocused beam line BL3 explain the discrepancy by the observation of a large source size, see section FEL Characterization.

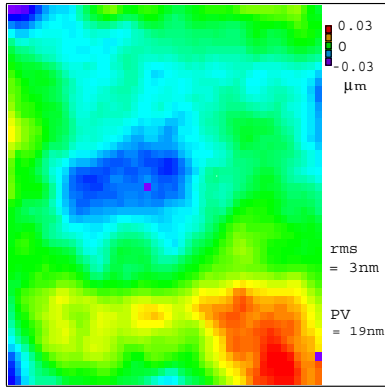


Figure 4: Full field of view (51 x 51 pixels) of a wave front. Displayed are the absolute discrepancies from a perfect wave front. The achieved result is close to the actual resolution limit of the used wave-front sensor.

Mirror alignment

A toroidal mirror with a focal length of 10 m is used at the beam line BL1. The critical alignment of the yaw angle is demonstrated in Figure 5. First the small field of view is obvious. Far from optimal for this kind of measurements it is due to the long focal distance of 10 m that we were forced to position the sensor only 2.55 m behind the focal spot, which leaves the here displayed beam size of $\sim 3\ \text{mm}$. Image (a) shows a strong astigmatism. The overall ellipsoidal beam profile is narrow and tilted. The rms of 395 nm only documented the obvious misalignment. From image (a) to image (b) in Figure 5 the toroidal mirror was moved by 5 mrad in the direction of the yaw angle. A strong change in beam profile and shape took place. The beam profile is more of the true circle of the FEL itself but still tilted. The rms of the distortions is 70 nm, only. The centre of the beam stays at the same pixel position than before. From image (b) to image (c) the mirror was further moved by 5 mrad around the yaw angle. Closer to an optimal alignment the improvement is not as drastic as it had been before. The shape of the beam stays the same and only its diagonal becomes a perfect horizontal line. Therefore the centre of the beam moved by 5 pixels in x and in y direction. The wave front is of $\text{rms}=50\ \text{nm}$. The detailed analysis of the best image (c) evaluated 73% of the distortions as

astigmatism caused by a wrong position in the yaw angle direction, and 12% as coma, due to a minor misalignment in the roll angle orientation. Further alignments are planned in the future after improvements, concerning the field of view and some mirror mechanics, took place. The wave-front measurements proved the need of such upgrades at beam line BL1.

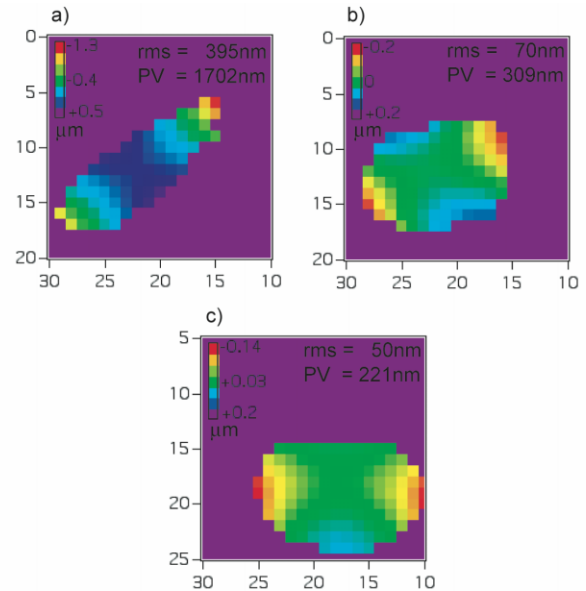


Figure 5: Wave front changes during the optimisation of the toroidal mirror in the direction of the yaw angle at beam line BL1. The scales are different for the images to identify the shape of each wave front. To document the position of the spot the illuminated pixels of the CCD are displayed, bottom and left. Between the images the mirror was tilted in the yaw direction by total 10 mrad.

Long-term documentation

In the last year the FLASH beam performance shown an incredible improvement. Especially the mean beam intensity increases by more than one order of magnitude. The long-term effects to the optical elements need to be observed. The highly sensitive wave-front measurements are excellent to show even slight damages to the carbon coating of the mirrors. No other diagnostic tool can provide us with such information during an operation mode of the FEL.

Filter performance

A FEL beam consists of higher harmonic parts. Less than 1% intensity of the fundamental can contribute in the third harmonic, the most intense higher harmonic. Nevertheless, orders up to the seventh harmonic were measured. The application of filters and filter systems is required to make detailed use of these lower wavelengths or to eliminate any ill effects for some experiments.

The standard used nitrogen gas absorber not influences the FEL wave front. This was checked during a FEL operation with a wavelength of 32 nm. The use of the absorber to a transmission of only 0.1% leaves the FEL wave front unchanged.

More critical is the use of solid filters, metal foils or crystalline membranes. A generally used thickness of such a filter is 200 nm. Up to now, no effect in this regime is recorded. To get a change in wave front an aluminium foil of $> 2 \mu\text{m}$ had to be put in the beam. Even then, the wave front distortions are homogenous and of only 13 nm rms. Therefore, the effect to the optical geometry by creating a second source component is of more consequent for an experiment.

This result eased the wave front measurements itself in the future, as the still complicated reactions on changes in intensity can be countered with additional filters without questioning the achieved results.

FEL CHARACTERIZATION

FLASH is the first working FEL in the EUV and soft x-ray regime [3, 4]. Source size, shape, and position can vary on a shot to shot characteristic. The importance for most beam line optics has been pointed out in the section above. Here the characteristic of the FEL itself and any conclusions considering the machine operation is discussed. The task is to evaluate the resolution of the sensor for the requirements at FLASH.

A good wave front of 4 nm rms was recorded at the end of beam line BL3 with four flat mirrors along the regular beam path. Relative measurements to a beam origin in a $50 \mu\text{m}$ pinhole in front of these mirrors lead to a portion of 2 nm rms caused by the optics and of 2 nm rms origins in the incident FEL beam. In this regime the measurements are close to the limit of the sensor calibration. Further, the shot to shot variations of the FEL pulses were observed with the same magnitude. To allow an analysis of such a beam we are in need of a better calibration of the sensor.

Similar limits are recorded concerning the source size and distance. In general the realistic value of 82 m distance to the source is reproduced. Nevertheless, the current setup and software can produce errors of some meters for a focal spot in a distance of more than 80 m. This is unacceptable by at least one order of magnitude.

The beam size at the experimental station of BL3 in February 06 was 10 mm fwhm. In a situation of not fully reached the saturation level such a large beam size is not surprising. The standard deviation of the x- and y-position of the beam centre was 1.3 mm and 2.3 mm respectively, translated in an angle of $\sim 24 \mu\text{rad}$. These results match the theoretical parameters of a FEL just close to saturation [3].

A qualitative measurement of relevant machine parameter is not resolved with the current wave-front sensor setup. Improvements are foreseen: First an automatic alignment of some equipment parts is planned to minimize the sensor alignment time in respect to the limited beam time available. In this context the diffraction limit of the sensor design $\lambda/120$ at 13 nm [5] shall be reached at the FEL, too. Therefore a new and perfect calibration is required. Thinkable is the use of a different Hartmann plate or the development of a new sensor

specialized for the different and progressed circumstances at a FEL facility like FLASH.

ONLINE IMPLEMENTATION

In contrast to other diagnostic tools the here-introduced sensor measured the wave front in a distance of some meters behind the focal spot. A use as online diagnostic is possible when the direct beam path is not blocked by the experiment itself, e.g. most experiments operating in the gas phase. Even if a target block the beam a verification of the FEL performance in between some measurements is useful.

Main problems are the intensity and geometric circumstances, which will be dictated by the experiment itself and not by the wave-front measurements anymore. As critical as these adaptations have been so far it is a challenge to provide a setup with even more flexibility.

CONCLUSION

The here reported measurements proved the feasibility of wave front observations under FEL conditions. The high sensitivity of the wave-front sensor is required for the high beam quality at FLASH. First order aberrations were recorded during first beam line commissioning. The ongoing improvement of the FLASH beam quality in stability, source size, and intensity as well as optimized optics alignment was documented during the last year. The non-invasive and remote sensor can be used as online tool to document the shot to shot characteristics of the FEL.

ACKNOWLEDGMENT

These measurements based upon the work of U. Hahn and the HASYLAB optics and vacuum groups. The commissioning is part of the FLASH team [3].

This work was supported by the European Community Research Infrastructure Action under the FP6 "Structuring the European Research Area" Programme through the Integrated Infrastructure Initiative "Integrating Activity on Synchrotron and Free Electron Laser Science", contract number RII3-CT-2004-506008.

REFERENCES

- [1] S. Le Pape, P. Zeitoun, M. Idir, P. Dhez, J. J. Rocca, M. Francois, Phys. Rev. Lett. vol. 88 (2002), p. 183901.
- [2] W. H. Southwell et al., JOSA, vol. 70 (1980) p. 8
- [3] V. Ayvazyan et al., Eur. Phys. J. D, vol. 37 (2006), p. 297.
- [4] E. L. Saldin, E. A. Schneidmiller, M. V. Yurkov, DESY Print TESLA-FEL, 2004-06 (2004).
- [5] P. Mercere, P. Zeitoun, M. Idir, S. Le Pape, D. Douillet, X. Levecq, g. Dovillaire, S. Bucourt, K. A. Goldberg, P. P. Naulleau, S. Rekawa, Optics Lett., vol. 28 (2003), p. 135.

A NEW GENERATION OF X-RAY OPTICS BASED ON PYROLYTIC GRAPHITE*

H. Legall, H. Stiel, Max-Born-Institute, Berlin, Germany

A. Antonov, I. Grigorieva, Optigraph GmbH, Berlin, Germany

V. Arkadiev, IAP e.V., Berlin, Germany

A. Bjeoumikhov, IfG GmbH, Berlin, Germany and A. Erko, BESSY GmbH, Berlin, Germany

Abstract

Highly Oriented Pyrolytic Graphite (HOPG) is a mosaic crystal, which consists of a large number of small nearly perfect crystallites. The unique structure of HOPG crystals enables them to be highly efficient in diffraction in an energy range between 2 keV up to several 10 keV. The mosaicity of the crystal is responsible for the dramatic increase of integral reflectivity in comparison to perfect crystals. Furthermore thin HOPG crystal films can be easily bent and exhibit a very high thermal conductivity making them interesting for application in experiments with high average power x-ray sources. For application in x-ray spectroscopy the achievable spectral resolution of the crystal optics is of particular interest. Recently performed measurements with very low foil thickness have revealed a spectral resolution of $E/\Delta E = 2900$ in (004)-reflection. This is by far the highest spectral resolution reported for Pyrolytic Graphite (PG) crystals. The integral reflectivity of these films is still comparable to that of ideal Ge crystals. In this work we present new results concerning the energy resolution, integral reflectivity and application of thin bent Graphite films.

INTRODUCTION

Highly oriented pyrolytic graphite (HOPG) is an artificial graphite produced by thermal cracking of a hydrocarbon gas and deposition under low pressure and afterwards annealing the deposit under pressure [1]. In this way and after some further fabrication steps thin films of HOPG can be made with thickness of less than $10 \mu\text{m}$. These films can be easily bent by mounting them adhesively on a mould of any shape [2].

Sectional topographical diffraction measurements have shown an arrangement of the small crystallites with some μm in size to larger mosaic blocks with some $100 \mu\text{m}$ in diameter and some $10 \mu\text{m}$ in thickness [3]. The angular distribution of the crystallites, with plane orientations off to the normal axis to the crystal surface, is called mosaic spread. The mosaic spread between the crystallites is much smaller than that between the mosaic blocks. The mosaic blocks again show a correlation in orientation and form larger crystal domains with some mm in size.

Because of its high thermal conductivity κ and low linear thermal expansion coefficient α in basal plane (cp. Ta-

ble 1), which both are similar to those of diamond crystals, PG crystals could be interesting for many applications with regard to x-ray sources delivering high average x-ray power. Also the absorption thickness t_{abs} of HOPG is similar to that of diamond. Consequently less heat is absorbed in comparison to other crystals.

The diffraction properties influencing the energy resolu-

Table 1: Thermal properties and absorption thickness at 8 keV for different crystals.

Material (hkl)	κ [W/cm K]	α [K x 10^{-6}]	t_{abs} [μm]
Diamond(111)	21	0.8	250
Si(111)	1.25	2.33	8.7
Ge(111)	0.58	5.9	2.94
HOPG(002)			239
(parallel (002))	17	1	
(perpendicular)	8	20	
HOPG(004)			477

tion of PG films are determined by the mosaicity and the intrinsic width of Bragg reflection. Latter refers to the diffraction properties of the small crystallites and is called the Darwin width for nearly perfect crystals. It results from particle size and/or strain broadening. Mosaicity makes it possible that even for a fixed angle of incidence to the crystal surface, an energetic distribution of photons can be reflected, because each photon of this energetic distribution can find a crystallite plane at the right Bragg angle. The width of this energetic distribution depends on the mosaic spread. The mosaicity is also responsible for the dramatic increase of integrated reflectivity in comparison to perfect crystals in an energy range between 2 keV and several 10 keV [4]. The so-called mosaic-focusing, as shown in Fig. 1, which occurs in a 1:1 magnification geometry enhances further the intensity in the image plane.

In contrast to ideal crystals, in mosaic crystals the photon has to penetrate deeper into the crystal, before it finds a crystallite aligned well, from which it can be reflected. That means that the effective depth, from which diffraction in mosaic crystals occurs, is much larger compared to ideal crystals. Therefore the energy resolution can be strongly affected by the thickness of the Graphite films. Recently we have shown that very thin Graphite films can reveal energy resolutions and integral reflectivity comparable to Ge(111) [5].

* Work supported by the German national program of supporting development, innovation and technology (ProFIT Programm zur Förderung von Forschung, Innovationen und Technologien, Land Berlin, #10126367) and the European found for regional development (EFRE).

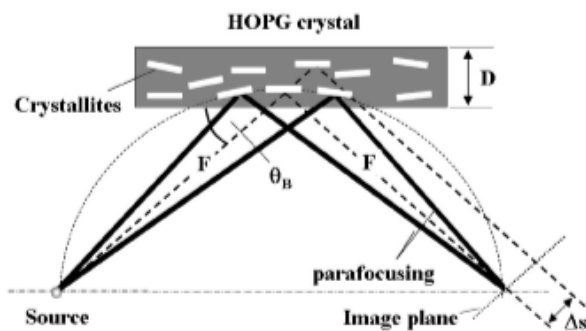


Figure 1: Diffraction properties of HOPG.

Because PG can be treated as an agglomeration of very small crystallites less strain is induced by bending the films and therefore no drastically changes of the diffraction properties determining the spectral energy resolution are expected and were measured up to now.

EXPERIMENTAL AND RESULTS

Samples

Two kind of HOPG crystals manufactured by Optigraph GmbH were investigated. Firstly, the well known "Highly Oriented Pyrolytic Graphite" (HOPG) crystal and secondly a new kind of HOPG crystal. This new material was already presented in [5]. Because the diffraction properties of the new material differ considerably from the well known HOPG it will be named by Optigraph henceforth "Highly Annealed Pyrolytic Graphite" (HAPG) to distinguish it from the commonly HOPG. This new kind of PG crystal is optimized for the application in x-ray spectroscopy by a modified fabrication process. To get a comprehensive overview over the relationship between energy resolution and thickness in flat and bent geometry, crystals with different thickness were measured in (004)-reflection in both geometries. To realize precise variations in thickness the PG films were fabricated by stacking thin 10 - 15 μm thick PG films. The influence of the stacking on the energy resolution was investigated by measuring also thicker PG films consisting of only one sheet. The flat crystals were mounted on polished glass plates and the bent crystals were mounted on a cylindrical polished lens with radius 150 mm. The thickness of the investigated films was determined with an accuracy of $\pm 5 \mu\text{m}$ using a micrometer screw before mounting them on the moulds. It must be noted, that the measured thickness is an averaged value. That means, that the thickness can vary slightly for different sites of the crystal.

Experimental setup

The experimental setup is shown in Fig. 2. It consists of the HOPG crystals, an x-ray tube and a CCD camera.

The x-ray source, which was used for the measurements, is a low power microfocus x-ray tube (IfG) with a source diameter of about 50 μm . Measurements were performed with the Cu K_{α} emission of a Cu anode at 8 keV. The spec-

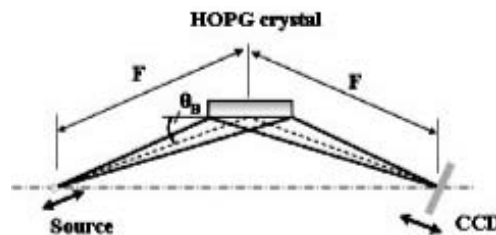


Figure 2: Experimental setup.

tra were collected with a 16-bit deep depletion CCD camera (Roper Scientific model PI-LCX 1300) with a quantum efficiency of about 50% at 8 keV. A thin (250 μm) Be window in front of the deep depletion CCD was used for vacuum sealing of the camera, so that a deep cooling (down to $-50 \text{ }^{\circ}\text{C}$) of the CCD was possible. The distance between source and crystal and between crystal and detector was $F = 400 \text{ mm}$ in each measurement. All measurements were carried out with the detector plane oriented perpendicularly to the reflected x-ray beam.

Results

In Fig. 3 selected images of the reflected Cu K_{α} emission are presented for both investigated PG crystals. In the upper image a 15 μm HAPG and in the lower image a 10 μm thick HOPG crystal in flat geometry is shown. As can be seen from the cross sections of the images in

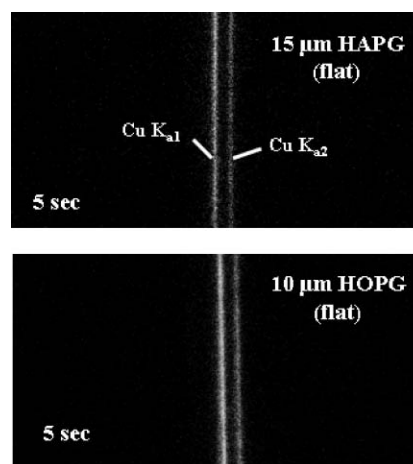

 Figure 3: Recorded images of the reflected Cu K_{α} emission from a 15 μm thick HAPG and a 10 μm thick HOPG.

Fig. 4 the measured energy resolution of the flat HAPG crystal is better than that of the HOPG crystal with nearly same thickness. The energy resolution was determined by a convolution procedure as described in [5]. From the convolution procedure an energy resolution $E/\Delta E$ of 4100 was

found for the 15 μm flat HAPG and 3500 for the 10 μm flat HOPG. The reflection broadening due to crystal thickness, which is in the range of a single mosaic block, cannot explain the difference in energy resolution between both crystals. Therefore, the differences in energy resolution are more likely a broadening due to the flat geometry of the crystals. Latter gives rise to a focusing error in the image plane, because the alignment of the mosaic blocks in the basal plane deviates from a Rowland circle. These so-called flat focusing error increases with mosaicity (cp. [6]). Hence for the HAPG lower mosaic spread can be expected. As mentioned above the 15 μm HAPG crystals are compa-

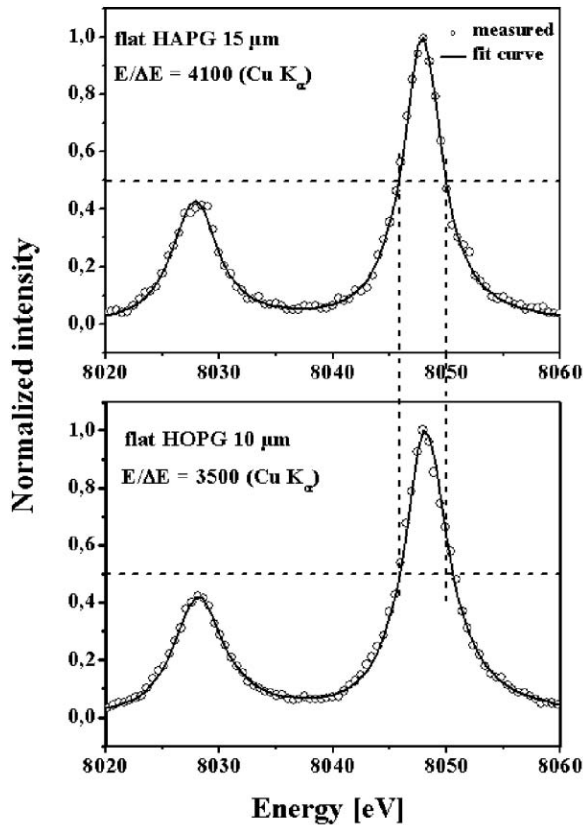


Figure 4: Cross sections of the recorded images in Fig. 3. The circles are measured points and the lines represents the fit curves of the convolution procedure.

table to the 15 μm thick crystal which was presented in [5]. The energy resolution in Fig. 4 is higher because the distance F is larger. Taking the values for the energy resolution from [5] and comparing these values with the measured energy resolution at 400 mm distance a nearly linear increase of energy resolution over distance is observed.

As already reported in [5] the integral reflectivity of the 15 μm thick HAPG in (004)-reflection is similar to that of Ge(111) crystals. For the 10 μm HOPG the integral count rate on the CCD over the Cu K_{α} emission is by factor two higher than that of the 15 μm HAPG.

The energetic reflection bandwidth of these thin 15 μm

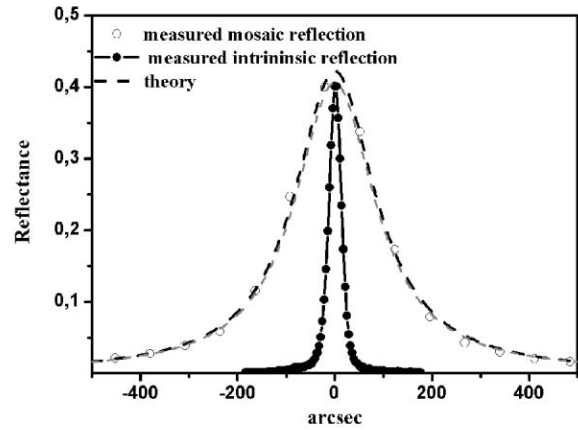


Figure 5: Measured rocking curves of a 15 μm thick HAPG crystal in (002)-reflection. The measurements of the rocking curves were performed using a triple-crystal diffractometer (BESSY).

HAPG films can be determined by rocking curve measurements. The measurements of the rocking curves were performed in (002)-reflection using a triple-crystal diffractometer at BESSY. In Fig. 5 the mosaic reflection and the intrinsic width of reflection of HAPG(002) are shown. The rocking curve width (FWHM) is 0,056 $^{\circ}$ for the mosaic reflection and 27 arcsec for the intrinsic reflection. From the mosaic reflection the mosaic spread can be determined. To determine the mosaic spread from the measured rocking curves a reflectivity formula [7] derived from Zachariassen's treatment was used [8]. The best fit was obtained with a Lorentzian distribution and a mosaicity of 0.042 $^{\circ}$. From the measured mosaic spread the energetic bandwidth can be calculated in both reflection orders.

To enhance the reflectivity the thickness of the HAPG

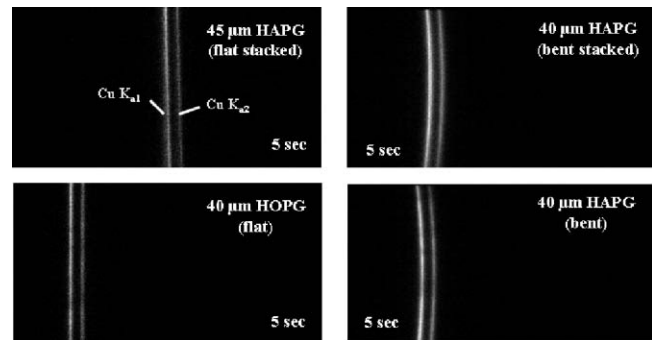


Figure 6: Recorded images of the reflected Cu K_{α} emission from a stacked 45 μm thick flat HAPG (upper left image), a 40 μm bent stacked HAPG (upper right image) and a 40 μm single sheet HAPG in flat (left lower image) and bent (right lower image) geometry.

films was increased. In Fig. 6 the images of a 40 μm thick

HAPG single sheet and a stacked HAPG of same thickness are shown. Due to thickness broadening the energy resolution drops down to 3300 for both sheets. In contrast the integral count rate increases by a factor 4 for both 40 μm PG films in comparison to the 15 μm thick film. Also shown in Fig. 6 are bent HAPG crystals of same thickness. Bending these 40 μm thick HAPG crystals revealed fully different energy resolutions. While bending increases the energy resolution for the single sheet of HAPG as shown in Fig. 7, for the stacked bent HAPG the energy resolution drops down to 2300 (not shown). This result was surprisingly and indicates maybe changes in the mosaic structure by bending. In the case of the stacked HAPG an interaction between different layer has to be taken into account.

Finally, to enhance further the integral reflectivity accom-

CONCLUSION

High energy resolution can be obtained in (004)-reflection using very thin PG crystals. These high energy resolutions are accompanied with high integral reflectivity. As shown, bending single sheets of these very thin crystals seems not to decrease the energy resolutions.

Because of its good thermal properties PG could be interesting for many different applications based on high averaged x-ray sources, as e.g. the Free Electron Laser. A very promising application for PG crystals could be the single shot x-ray spectroscopy in an energy range between several keV up to several 10 keV. This can be done with PG because the mosaic spread enables to record a broad energy range with high energy resolution in a single shot.

REFERENCES

- [1] A.W. Moore, "Chemistry and Physics of Carbon", Vol. 11, New York:Marcel Dekker (1973) 69-187.
- [2] I.G. Grigorieva, A.A. Antonov, X-Ray Spectrometry 32(1) (2003) 64-68.
- [3] M. Ohler, M. Sanchez del Rio, A. Tuffanelli, M. Gambacini, A. Taibi, A. Fantini and G. Pareschiet, J. Appl. Cryst. 33 (2000) 1023-1030.
- [4] A. K. Freund, A. Munkholm and S. Brennan, Proc. SPIE 2856 68-81.
- [5] H. Legall, H. Stiel, V. Arkadiev, and A. A. Bjeoumikhov, Opt. Expr. 14 (2006) 4570-4576.
- [6] G. E. Ice and C. Sparks, J.Nucl. Instrum. Methods A 291 (1990) 110-116.
- [7] G.E. Bacon and Lowde R.D., Acta Cryst. 1 (1948) 303-314.
- [8] W.H. Zachariasen, "Theory of X-Ray Diffraction in Crystals", New York:Dover (1945).

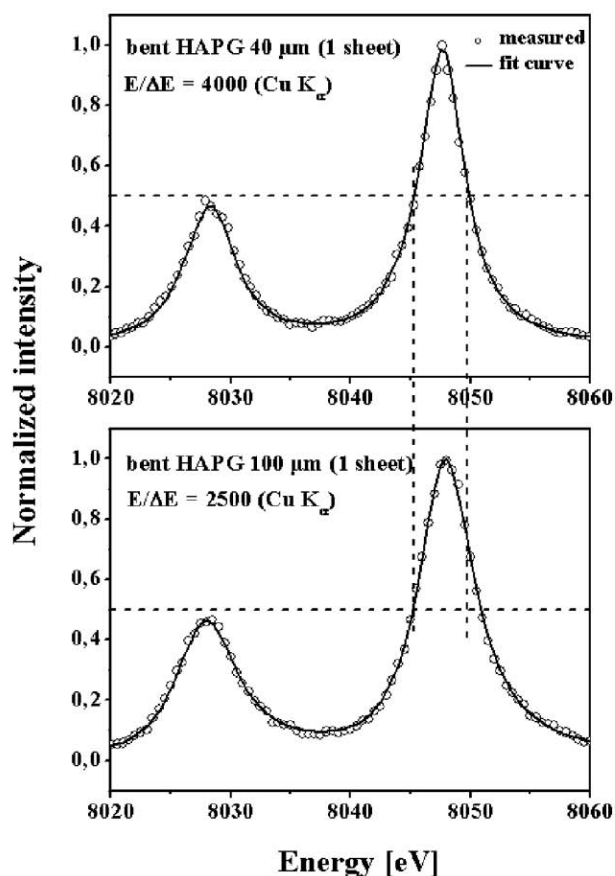


Figure 7: Cross sections of the recorded images in Fig. 6. The circles are measured points and the lines represents the fit curves of the convolution procedure.

panied with high energy resolution a 100 μm thick single HAPG sheet was investigated. The integral count rate increases further by a factor 2 and the energy resolution drops down to 2500 as can be seen in Fig. 7.

QUANTITATIVE DETECTION OF FEMTOSECOND X-RAY PULSES

Mathias Richter, Levent Cibik, Udo Kroth, Michael Krumrey, Hendrik Schoeppe,
Gerhard Ulm, PTB, Berlin;

Christian Blome, Ulf Jastrow, Jochen Schneider, Kai I. Tiedtke, Thomas Tschentscher, DESY, Hamburg;
Sergey Bobashev, IOFFE, St. Petersburg; Andrei Sorokin, PTB, Berlin, IOFFE, St. Petersburg;
Jerome Hastings, Rasmus Ischebeck, Stefan Moeller, SLAC, Menlo Park, California

Abstract

A detection system for femtosecond X-ray pulses has been developed within close cooperation between the Deutsche Elektronen-Synchrotron in Hamburg and the Physikalisch-Technische Bundesanstalt in Berlin. It is based on photoionization of Xenon gas and, hence, radiation hard. Photoions generated are extracted by an electric field and, in contrast to former devices developed for the vacuum-ultraviolet spectral range¹, detected by an amplifying open electron multiplier. Operation is performed at low gas pressure in the range between 0.1 and 0.01 Pa. Thus, the detector is almost transparent and may be used as a fast online monitor for quantitative and pulse-resolved determination of photon numbers and pulse energies of X-ray free electron lasers. After design and construction, a prototype has been successfully characterized and calibrated for photon energies from 4 to 10 keV in the PTB laboratory at the electron storage ring BESSY II in Berlin. First application has recently been realized in collaboration with the Linear Coherent Light Source at the Sub-Picosecond Pulse Source in Stanford with up to $1 \cdot 10^6$ photons per pulse detected at a photon energy of 9.4 keV.

**PAPER NOT
AVAILABLE**

¹M. Richter et al., Appl. Phys. Lett. 83, 2970-2972 (2003)

SCIENCE AT SINGLE PASS X-RAY FREE ELECTRON LASERS

J.R. Schneider, DESY, Hamburg

Abstract

Based on recent experience gained at the Free Electron Laser in Hamburg (FLASH) operating in the spectral range of the VUV, the first free electron laser user facility world wide, the requirements for successful experiments will be discussed. This includes the interplay between experimentalists on one and accelerator physicists and operators on the other hand, the need for various diagnostic tools, samples and sample environment, as well as the need for new approaches for data analysis

**PAPER NOT
AVAILABLE**

ONE- AND TWO-COLOUR PHOTOIONIZATION EXPERIMENTS AT FLASH

M. Meyer, LIXAM, Orsay

Abstract

Photoionization processes induced by femtosecond extreme-ultraviolet (XUV) pulses of the Free Electron Laser in Hamburg (FLASH at DESY) were investigated in He, Ar, Kr and Xe by means of photoelectron spectroscopy. The well-known photoionization cross sections of rare gases enabled us to determine for each individual FEL pulse the importance of higher orders (0.5 - 1%) of the fundamental wavelength (32, 25 or 13.7 nm)¹. In a second series of experiments, the FEL was combined with a synchronized optical laser of 12 ps or 120 fs temporal width. ATI (Above Threshold Ionization) processes induced by the optical laser are giving rise to 'sidebands' in the photoelectron spectrum. Their intensity exhibits a characteristic dependence on the relative time delay between both pulses and provides an inherent time marker for time-resolved pump-probe experiments. The results are in excellent agreement with theoretical predictions and allow a first analysis of two-colour ionization processes². Finally, the temporal stability, i.e. the jitter of the FEL pulses with respect to the optical laser, was determined by measuring cross correlation curves with the ps- (523 nm) or the fs-laser (800 nm).

**PAPER NOT
AVAILABLE**

¹S. Düsterer et al., Opt. Lett. 31, 1750 (2006)

²M. Meyer et al., Phys. Rev. A (Rap. Comm.) submitted.

ULTRAFAST COHERENT DIFFRACTION IMAGING WITH X-RAY FREE-ELECTRON LASERS*

H. N. Chapman[#], S. Bajt, A. Barty, W.H. Benner, M.J. Bogan, M. Frank, S.P. Hau-Riege, R.A. London, S. Marchesini, E. Spiller, A. Szöke, B.W. Woods, LLNL, Livermore, CA 94550, U.S.A.

J. Hajdu[†], M. Bergh, F. Burmeister, C. Caleman, G. Huldt, F.R.N.C. Maia, M.M. Seibert, D. van der Spoel, U. Uppsala, S-75124 Uppsala, Sweden.

S. Boutet, K.O. Hodgson, SSRL, SLAC, Menlo Park, CA 94305, U.S.A.

D.A. Shapiro, CBST, UC Davis, Sacramento, CA 95817, U.S.A.

Abstract

The ultrafast pulses from X-ray free-electron lasers will enable imaging of non-periodic objects at near-atomic resolution [1]. These objects could include single molecules, protein complexes, or virus particles. The specimen would be completely destroyed by the pulse in a Coulomb explosion, but that destruction will only happen after the pulse. The scattering from the sample will give structural information about the undamaged object. There are many technical challenges in carrying out such experiments at an XFEL. We are addressing some of these challenges with experiments at the FLASH soft-X-ray FEL at DESY.

SINGLE PARTICLE IMAGING

The success of crystallography lies in its ability to overcome radiation damage by spreading the X-ray dose over many ($> 10^9$) identical copies of the molecule and by taking advantage of the strong signal that arises from the coherent superposition of X-rays within Bragg spots. However, by performing measurements with ultrashort pulses, we can apply crystallographic techniques to non-repetitive structures (including cells, viruses, and single macromolecules). The radiation dose required for such “diffraction imaging” will be orders of magnitude above the steady-state damage threshold of about 200–4000 photons/Å² (depending on sample size and wavelength) [2]. Even so, the high-angle (high-resolution) scattering from a single molecule will be extremely weak since,

unlike diffraction from a crystal, there will be no coherent addition of scattering from many identical unit cells. We expect that the proposed XFELs will provide enough photons per pulse to give a measurable atomic-resolution signal.

Atomic-resolution imaging of biological objects with X-rays will necessarily be “lensless”; a diffraction pattern is recorded and a computer reconstruction algorithm performs the image formation step, replacing the role of a lens. Although the phase (wavefront) of the diffraction pattern is not recorded, it is possible to reconstruct the complex-valued image of a finite object from the far-field diffracted intensity. For single molecules and other non-periodic objects, the diffracted intensity is not confined to Bragg spots as it is for crystals. This allows an “oversampling” of the diffraction pattern, and the collection of information not accessible in a crystallographic experiment [3,4]. The “shrinkwrap” algorithm [5] is a particularly robust and practical method of using this information and performing 2D and 3D image reconstructions [6].

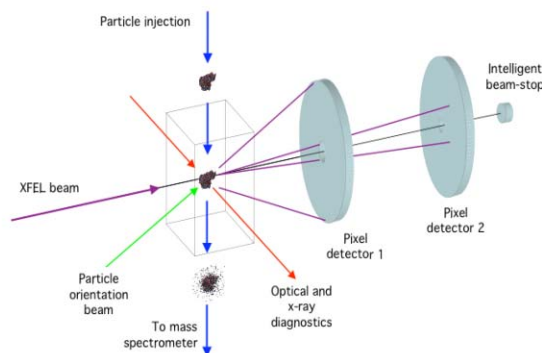


Figure 1: Schematic diagram of a single-particle diffraction imaging experiment at an XFEL.

*Work supported by U.S. Department of Energy (DOE) under Contract W-7405-Eng-48 to the University of California, Lawrence Livermore National Laboratory; the National Science Foundation Center for Biophotonics, University of California, Davis, under Cooperative Agreement PHY 0120999; The National Center for Electron Microscopy and the Advanced Light Source, Lawrence Berkeley Lab, under DOE Contract DE-AC02-05CH11231; Natural Sciences and Engineering Research Council of Canada; the U.S. Department of Energy Office of Science to the Stanford Linear Accelerator Center; the European Union (TUIXS); The Swedish Research Council; The Swedish Foundation for International Cooperation in Research and Higher Education; and The Swedish Foundation for Strategic Research.

[#]henry.chapman@llnl.gov

[†]janos.hajdu@xray.bmc.uu.se

A full 3D reconstruction can be achieved from diffraction patterns taken from many different orientations of the structure. With an XFEL, a complete data set will require identical copies of the object exposed to the beam one by one, which may be injected into the vacuum environment of the experiment and pass through the beam path at a random orientation. With identical samples it will be possible to sort diffraction patterns to find those of similar orientation that can then be averaged. The averaging step will be important in order to improve the signal to noise ratio (SNR) and hence improve resolution. The critical step in the analysis becomes finding the minimum dose that is required not to image a particle, but to infer its orientation. Hence any method that can be employed to fix a particle's orientation, such as laser alignment [7,8] will have a big impact on the success of the technique.

A concept of the single-particle diffraction experiment is shown in Fig. 1. Some of the challenges we face to develop this technique include: understanding the interaction of the specimen and the FEL pulse to determine how short a pulse is required to overcome radiation damage; methods to focus X-ray FEL pulses to below 0.1 micron focal spots to achieve high intensity; development of high-dynamic range, low noise, and fast area detectors; methods of delivering purified samples into the beam without containers or substrates; handling the large data stream from the detectors and performing the classification and averaging of the diffraction data; and developing robust 3D imaging techniques.

RESOLUTION LIMITS

Radiation Damage

Radiation damage significantly limits the resolution of conventional imaging experiments. Damage is caused by energy deposited into the sample by the probes used for imaging (photons, electrons, neutrons, etc.). Cooling can slow down sample deterioration, but it cannot eliminate damage-induced sample movement *during* conventional measurements [9-12]. Ultra short x-ray pulses from X-ray free-electron lasers offer the possibility to extend the conventional damage limits, and will allow the imaging of non-crystalline biological (and other) materials. For proteins, simulations based on molecular dynamics (MD) [1, 13, 14], hydrodynamic [15, 21], and on plasma models [16] indicate that if very short (100 fs or less) and very intense x-ray pulses are available ($\geq 10^6$ photons/Å² on the sample), then a single scattering pattern could be recorded from a single protein molecule in the gas phase before radiation damage manifests itself and ultimately destroys the sample (Figure 2).

The hydrodynamic (HD) model can be computed fast on a computer, as compared with MD models. However, the MD models are potentially more accurate since they treat the microscopic atom-atom and atom-electron interactions in greater detail. The general approach at our laboratories is to use HD for simulations of the soft x-ray experiments at FLASH and to quickly explore new

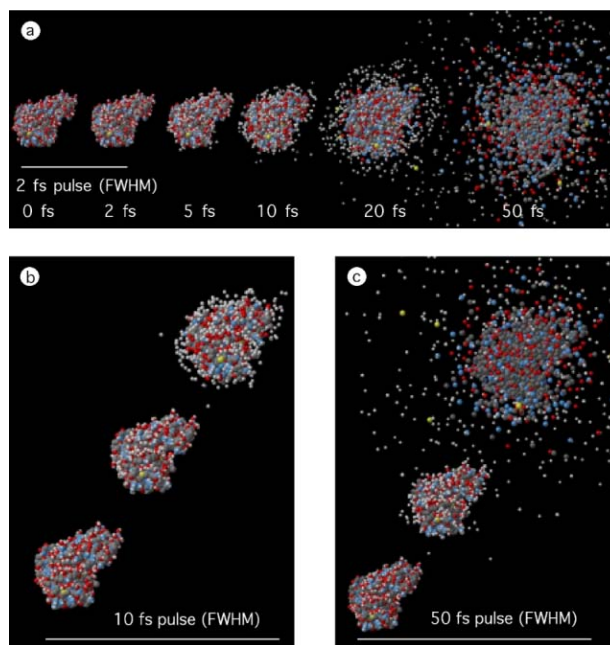


Figure 2: MD simulation of radiation-induced Coulomb explosion of a small protein (lysozyme). White balls: H, Gray: C, Blue: N, Red: O, Yellow: S. Integrated X-ray intensity: 3×10^{12} (12 keV) photons/100 nm diameter spot (corresponding to 3.8×10^8 photons/nm², or 3.8×10^6 photons/Å² on the sample) in all cases. (a) Protein exposed to a 2 fs FWHM X-ray pulse, and disintegration followed in time. The atomic positions in the first two structures (before and after the pulse) are practically identical at this pulse length due to an inertial delay in the explosion. (b) Lysozyme exposed to the same number of photons as in (a) but the pulse FWHM is now 10 fs. The images show the structure at the beginning, in the middle and near the end of the X-ray pulse. (c) Behaviour of the protein during a 50 fs FWHM X-ray pulse. It is also apparent from the figure that during the Coulomb explosion, hydrogen ions and highly ionised sulphurs are the first to escape the immediate vicinity of the protein (at 12 keV, the photoelectric cross section for sulphur is about fifty times larger than that for carbon). Based on Neutze et al. [1].

concepts for molecular imaging at XFELs, while developing an advanced MD model including electrons for more accurate simulations of the x-ray-molecule interaction for XFELs.

The basic assumption of the HD model is that the sample can be described by a liquid-like continuum of matter rather than considering individual atoms. This gives a simplified description of the average effects of x-ray material interaction and atomic motion, which then permits calculations even on very big samples. The model further assumes that the particle is spherically symmetric, reducing the mathematical model to one dimension plus time. The model assumes that the motion of the atoms within the molecule is solely in the radial direction. The electrons and the atoms are treated as separate, structureless, fluids that interact through the Coulomb

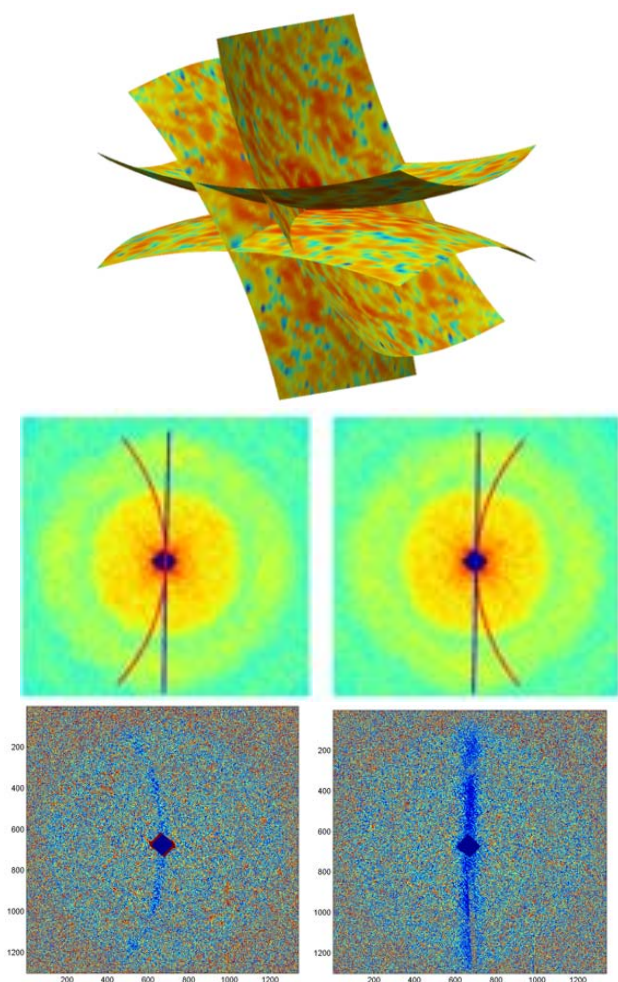


Figure 3: Intersection of two Ewald spheres with their centrosymmetric opposites. Centrosymmetry gives an extra intersect as there are *two* common arcs of intersection in *each* diffraction pattern (middle). The patterns in the middle show the expected arcs of intersections in two diffraction patterns from the experimental pyramid X-ray diffraction data set from Figure 10. Patterns at the bottom show these very lines of intersections when the experimentally obtained patterns are subtracted from each other pair wise (Huldt et al., in preparation).

force and ionization processes. The short-range electron-electron interactions are treated as a hydrodynamic pressure, and the long-range electron-electron and electron-ion Coulomb interactions are determined from the continuous net charge of the electrons and ions. In this model, all forces act radially. The model further assumes that the trapped electrons are thermalised among themselves, and that they are inertia free, so that they quickly relax to a force-free spatial equilibrium. Finally, the x-ray matter interaction, atomic ionization processes, and energy of the trapped electrons are described by time-dependent rate equations. The model shows that at later phases in an exposure, trapped electrons quickly relax in

energy and position to form a cloud around the positive ions, leaving a neutral core and a positively charged outer shell (similar to Debye shielding). This layer is ejected first from the particle, and the Coulomb explosion proceeds from the outside in. A rarefaction wave propagates in from the surface at the sound speed, and hence the centre of the particle undergoes destruction later. In the inner core, there is hardly any ion motion but the high electron temperature leads to ionization and blurring of the electron density.

This behaviour has led to the proposal of a tamper as a sacrificial layer that will delay the onset of damage on the structure of interest [17]. The tamper may be a small water or helium drop that surrounds the molecule, and which has a total mass comparable to that of the molecule. Modern electrospray techniques can precisely control the amount of solvent left around the molecule and can be used to select an optimum layer thickness.

Sample reproducibility and orientation

Each particle (macromolecule) is exposed to the beam only once, and disintegrates at the end of this process. The diffraction pattern so recorded encodes a two-dimensional projection image of the sample (and this may provide sufficient information for some applications). Three-dimensional imaging requires more than one view from the sample. In addition, the signal-to-noise ratio of raw diffraction images will probably be insufficient for a high-resolution reconstruction, and it will be necessary to obtain a redundant data set so that averaging can enhance the signal. One could extend the depth of view from a single exposure by various holographic techniques based on external or internal reference beams, but a full three-dimensional reconstruction will most likely require *reproducible samples* exposed to the beam one-by-one, and in different orientations. A “reproducible sample” (e.g. purified proteins) may contain heterogeneities, different subgroups of sample, and distinct conformers of the molecule. How reproducible is a “reproducible sample” and how well can we distinguish between similar and dissimilar structures will affect resolution through a B-factor-like component.

Conventional “single molecule” electron cryo-microscopy [18,19] faces similar challenges as those described here. The basic requirement for reconstruction and/or signal averaging from many diffraction images is the ability to tell whether two noisy diffraction patterns represent the same view of the sample or two different views [20]. Huldt *et al.* [20] have shown that a signal of less than one photon per pixel would be sufficient to correlate diffraction images of identical particles presenting the same view, assuming photon noise only. Correlation-based methods to average and orient large numbers of noisy, randomly oriented real-space images have been successfully developed in the electron microscopy community [18,19]. Diffraction patterns are first classified into classes of like-orientation so that they can be averaged to increase the signal relative to noise. The average signal per diffraction pattern at the highest

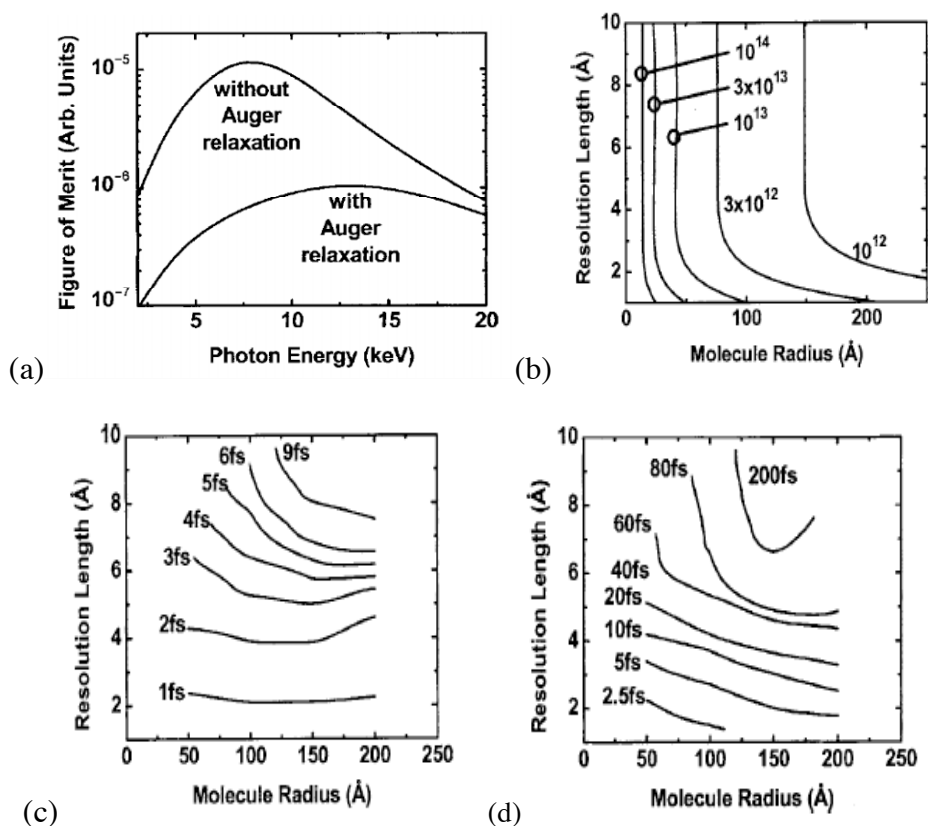


Figure 4: Resolution vs. radius for different X-ray fluences. (a) FOM for imaging conditions as a function of photon energy. (b) X-ray fluence requirements to classify two-dimensional diffraction patterns of biological molecules according to their orientation with 90% certainty. The curves are labeled with the X-ray fluence in units of photons in a 100 nm spot. (c) Plot of achievable resolution vs. molecule size for various pulse durations as limited by damage and classification. Atomic resolution imaging is achievable with pulse durations less than 5 fs and fluences greater than 10^{12} photons per 0.1 micron spot size. (d) Pulse duration requirements are significantly relaxed for samples that give 10 times larger scattering signal (e.g. viruses or nanocrystals) [21].

resolution, required for classification, is found to be much less than one photon per pixel, and an incident fluence of 10^8 ph/nm² is sufficient to achieve atomic resolution for particles greater than 15 nm radius [20].

Averaged diffraction patterns must be oriented with respect to each other in 3D Fourier space, which may be achieved by the method of common lines, a technique widely used in electron microscopy, where the micrographs represent planar sections through the center of the molecular transform. X-ray diffraction patterns are recorded on the Ewald sphere and so two patterns of different orientations will intersect along an arc in reciprocal space that passes through the zero spatial frequency. If the signal is strong enough for the line of intersection to be found in two averaged images, it will then be possible to establish the relative orientation of these patterns. We note that due to the curvature of the sections (especially at X-ray wavelengths), the common arc will provide a three-dimensional fix rather than a hinge-axis. Moreover, since the electron density of the object is real, its molecular transform exhibits centrosymmetry. This symmetry ensures that we obtain

two independent repeats of the common lines in the two images. This feature provides redundancy for determining sample orientation, and is unique to diffraction patterns (Figure 3).

Resolution for reproducible particles

A combination of results from the hydrodynamic continuum model [15] with the diffraction pattern classification model of Huld et al. [20] allows one to map out the landscape of imaging resolution, molecule size and pulse requirements [21]. The results are shown in Figure 4, which show that it will be possible to image single molecules at very high resolutions with very short pulse durations (atomic resolution with pulses less than about 5-10 fs).

First, the optimal photon energy for diffraction imaging was estimated by maximizing a figure of merit (FOM), defined as the ratio of signal minus noise to the radiation damage. As shown in Figure 4a, for pulses shorter than the Auger decay time (~ 10 fs for C), the optimum photon energy is 8 keV, and for longer pulses it is 13 keV, although the peak FOM is much smaller. Figure 4b shows

the required x-ray fluence versus image resolution length and particle radius, required to achieve a large enough diffraction signal to classify the patterns. Figure 4c shows the pulse length requirements for x-ray imaging biological molecules with 12 keV photons, assuming no pre-orientation of the molecules. When the fluence requirements are relaxed by orienting molecules with laser fields, using nanocrystals containing only a small number of molecules, or helical molecules, or icosahedral virus particles up to 10-20 times longer pulses can be tolerated, see Figure 4d.

IMAGE RECONSTRUCTION

A number of methods exist for recovering phases for objects that have a finite size, or “support”. These include oversampling of continuous molecular transforms [4,22-25], holographic imaging methods [26-28], holographic data evaluation methods [29,30], classical methods of crystallography, and techniques for phase extension from lower resolution electron/X-ray cryo-microscopy images.

The past few years have seen the development of robust algorithms in solving the phase problem through oversampling the diffraction pattern, and this seems to be a most promising technique for the future. The 3D diffraction transform of a non-periodic particle is continuous. Only the diffraction amplitudes are sampled at discrete points by the pixellated detector and the process of classification. The measured diffraction intensities are proportional to the modulus squared of the Fourier transform of the wave exiting the object. On their own, these diffraction intensities are insufficient to back-transform to form an image in real space. That inversion requires knowledge of both the diffraction intensity and phase. If the diffraction pattern intensities are sampled finely enough, then it is possible to solve for the diffraction pattern phases [22,23]. The solution to this non-linear inversion problem is usually obtained iteratively by sequentially enforcing known constraints in reciprocal space and in real space. Specifically, in real space we assert that the image has zero scattering strength outside the area of the object’s boundary (called its support) [23], whilst in reciprocal space the squared modulus of the Fourier transform of the image must equal the measured diffraction intensities. Such algorithms have now been used successfully for image reconstruction in X-ray diffraction experiments [4-6,31-34]. An example of a reconstructed 3D image is shown in Figure 5.

The algorithms usually require that the support of the object be known *a priori*, and the closer the support to the actual object boundary, the better the reconstruction. The algorithm called SHRINKWRAP successively refines an estimate of the support from a current estimate of the image [5]. This algorithm does not require the support to be known and is remarkably robust at finding the smallest image support that contains the majority of the image intensity.

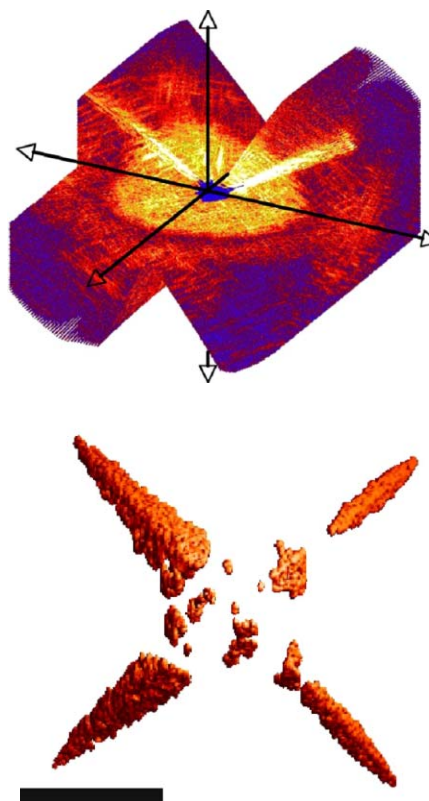
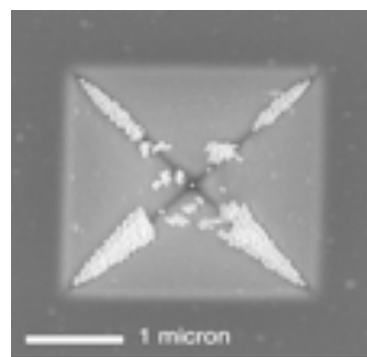


Figure 5: Coherent diffraction imaging and image reconstruction [6]. Three-dimensional diffraction data (middle) recorded from a test object (top), consisting of 50-nm diameter gold balls on a silicon-nitride pyramid-shaped membrane, at a wavelength of 1.6 nm, and a rendering of the *ab initio* 3D image (bottom) reconstructed from the diffraction intensities to a resolution of 10 nm. The diffraction data were obtained by rotating the specimen in 1° increments from -70° to $+70^\circ$, and then interpolated onto a 1024^3 -element array. A quadrant of the diffraction dataset has been removed for visualization in the central rendering of the 3D diffraction intensities. The gold balls seen in the rendering of the 3D reconstructed image on the right fill the inside edges of the silicon-nitride pyramid. The scale bar is 1 micron.

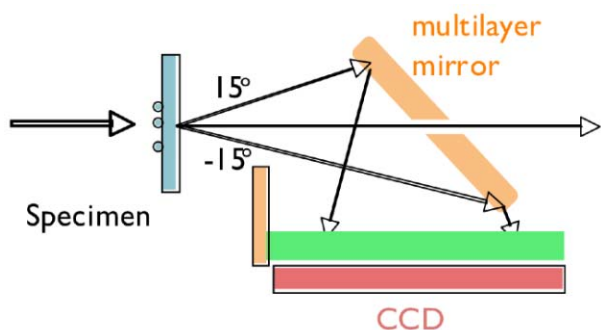


Figure 6: Schematic diagram of the diffraction camera for FLASH experiments, which uses a multilayer-coated mirror to reflect the diffraction pattern onto a CCD. The intense direct beam passes through a hole in the mirror.

EXPERIMENTS AT FLASH

Experiments were carried out at FLASH (Free-electron LASer at Hamburg, formerly known as the VUV-FEL). During the experiments the machine operated at a wavelength of 32 nm and in the ultrafast pulse mode of 25 ± 5 fs duration [36]. The pulses were focused to a $20 \mu\text{m}$ spot on the sample by an ellipsoidal mirror [37], achieving intensities up to about 10^{14} W/cm^2 . We carried out experiments to demonstrate ultrafast coherent diffraction imaging and to study the interaction of matter with FEL pulses, in order to constrain our models to determine ultimate resolution limits with XFELs.

Our experiments at FLASH depend critically on being able to measure the forward scattering from samples with high sensitivity and low noise or parasitic scattering. The main experimental challenge was to prevent the direct beam from hitting the direct-detection CCD and to prevent out of band radiation (plasma emission from the sample) or non-sample scatter from obscuring the coherent diffraction signals. We solved these problems using a flat mirror oriented at 45° to the beam. The direct beam passes through a hole in the mirror whereas the diffracted beam is reflected from the mirror onto a bare CCD. The camera records diffraction angles between -15° to $+15^\circ$, which requires a multilayer coating on the mirror that varies in layer spacing by a factor of two over a distance of only 28 mm (Bajt et al, in preparation). The multilayer coating was challenging because of the low absorption length of materials at 32 nm wavelength. We designed a coating consisting of three layers (Si, Mo, and B_4C), which simultaneously met the requirements of low stress, high reflectivity at 32 nm, and high reflectivity at the characterization wavelength of 0.154 nm. An advantage of the multilayer mirror is that it acts as a bandpass filter both for wavelength and direction. Plasma emission from the sample in the UV and visible ranges is rejected by the mirror. Stray light, from the scattering of beamline optics for example, hits the mirror at an angle

that does not obey the Bragg law, and hence are also filtered out. Additionally, the mirror reflectivity diminishes smoothly to zero at the edge of the hole, due to roughness of the substrate at the edge. This “soft edge” reduces scatter from the hole.

We have performed several experiments using this apparatus, which will be reported on in forthcoming publications.

REFERENCES

- [1] Neutze, R. Wouts, D. van der Spoel, E. Weckert, and J. Hajdu, “Potential for biomolecular imaging with femtosecond X-ray pulses,” *Nature* 406 (2000) 752.
- [2] D. Sayre and H.N. Chapman, “X-ray microscopy,” *Acta Cryst. A.* 51 (1995) 237.
- [3] D. Sayre, “Some implications of a theorem due to Shannon,” *Acta Cryst.* 5, (1952) 843.
- [4] J. Miao, P. Charalambous, J. Kirz and D. Sayre, “Extending the methodology of x-ray crystallography to allow imaging of micrometre-sized non-crystalline specimens,” *Nature* 400 (1999) 342.
- [5] S. Marchesini *et al.* “X-ray image reconstruction from a diffraction pattern alone,” *Phys. Rev. B* 68 (2003), 140101.
- [6] H.N. Chapman *et al.* “High-resolution ab initio Three-dimensional X-ray Diffraction Microscopy,” *J. Opt. Soc. Am. A* 23 (2006) 1179.
- [7] J.C.H. Spence and R. B. Doak, “Single molecule diffraction,” *Phys. Rev. Lett.* 92 (2004) 198102.
- [8] D. Starodub *et al.* “Damped and thermal motion of laser-aligned hydrated macromolecule beams for diffraction,” *J. Chem. Phys* 123 (2005) 24430.
- [9] R. Henderson, “Cryoprotection of protein crystals against radiation-damage in electron and X-ray diffraction,” *Proc. R. Soc.* 241 (1990) 6.
- [10] R. Henderson, “The potential and limitations of neutrons, electrons and X-rays for atomic resolution microscopy of unstained biological molecules,” *Quart. Rev. Biophys.* 28 (1995) 171.
- [11] C. Nave, “Radiation damage in protein crystallography,” *Rad. Phys. Chem.* 45 (1995) 483.
- [12] M.R. Howells *et al.*, “An assessment of the resolution limitation due to radiation-damage in x-ray diffraction microscopy,” <http://arxiv.org/physics/0502059>
- [13] Z. Jurek, G. Faigel, and M. Tegze, “Dynamics in a cluster under the influence of intense femtosecond hard x-ray pulses,” *Euro. Phys. J. D* 29 (2004) 217.
- [14] Z. Jurek, G. Oszlanyi and G. Faigel, “Imaging atom-clusters by hard x-ray free electron lasers,” *Europhys Lett.*, 65 (2005) 491.
- [15] S.P. Hau-Riege, R.A London and A. Szöke, “Dynamics of X-Ray Irradiated Biological Molecules,” *Phys. Rev. E* 69 (2004) 051906.
- [16] M. Bergh, N. Timneanu and D. van der Spoel, “A Model for the Dynamics of a Water Cluster in an X-ray Free Electron Laser Beam,” *Phys. Rev. E* 70 (2004) 051904.

- [17] R.A. London, A. Szöke, and S.P. Hau-Riege, "A tamper to delay the motion of a sample during irradiation by short intense x-ray pulses," patent pending (2006).
- [18] J. Frank, "Three-Dimensional Electron Microscopy of Macromolecular Assemblies," Academic Press, San Diego (1996).
- [19] M. van Heel *et al.* "Single-particle electron cryo-microscopy: towards atomic resolution," *Quart. Rev. Biophys.* 33 (2000) 307.
- [20] G. Huldt, A. Szöke and J. Hajdu, "Diffraction imaging of single particles and biomolecules," *J. Struct. Biol.* 144 (2003) 219.
- [21] S.P. Hau-Riege, R.A. London, G. Huldt and H.N. Chapman, "Pulse requirements for x-ray diffraction imaging of single biological molecules," *Phys. Rev. E* 71 (2005) 061919.
- [22] R.H.T. Bates, "Fourier phase problems are uniquely solvable in more than one dimension. 1. Underlying theory," *Optik* 61 (1982) 247.
- [23] J.R. Fienup, "Phase retrieval algorithms-a comparison," *Appl. Opt.* 21 (1982) 2758.
- [24] D. Sayre in *Proceedings of the 1990 NATO Course, Erice* (H. Schenk, ed.) (1991) p.353.
- [25] A. Szöke, "Time-resolved holographic diffraction at atomic resolution," *Chem. Phys. Letts.* 313 (1999) 777.
- [26] A. Szöke, "X-ray and electron holography using a local reference beam," in *Short Wavelength Coherent Radiation: Generation and Application*. Attwood, D. T. and Bokor, J. eds., American Institute of Physics Conference Proceedings No. 147, New York (1986).
- [27] M. Tegze and G. Faigel, "Atomic-resolution X-ray holography," *Europhys. Lett.* 16 (1991) 41.
- [28] M. Tegze and G. Faigel, "X-ray holography with atomic resolution," *Nature* 380 (1996) 49.
- [29] A. Szöke, "Holographic methods in X-ray crystallography. 2. Detailed theory and connection to other methods of crystallography," *Acta Cryst. A* 49 (1993) 853.
- [30] A. Szöke, H. Szöke and J.R. Somoza, "Holographic methods in X-ray crystallography 5. Multiple isomorphous replacement, multiple anomalous dispersion and non- crystallographic symmetry," *Acta Cryst. A* 53 (1997) 291.
- [31] I.K. Robinson, I.A. Vartanyants, G.J. Williams, M.A. Pfeifer and J.A. Pitney, "Reconstruction of the shapes of gold nanocrystals using coherent x-ray diffraction," *Phys. Rev. Lett.*, 87 (2001) 195505.
- [32] H. He, S. Marchesini, M. Howells, U. Weierstall, G. Hembree, and J. C. H. Spence, "Experimental lensless soft-x-ray imaging using iterative algorithms: phasing diffuse scattering," *Acta Cryst. A* 59 (2003) 143.
- [33] G. J. Williams, M. A. Pfeifer, I. A. Vartanyants, and I. K. Robinson, "Three-dimensional imaging of microstructure in Au nanocrystals," *Phys. Rev. Lett.* 90 (2003) 175501.
- [34] J. Miao, T. Ishikawa, E. H. Anderson, and K. O. Hodgson, "Phase retrieval of diffraction patterns from noncrystalline samples using the oversampling method," *Phys. Rev. B* 67 (2003) 174104.
- [35] D. Shapiro, P. Thibault, T. Beetz, V. Elser, M. Howells, C. Jacobsen, J. Kirz, E. Lima, H. Miao, A. M. Neimann, and D. Sayre, "Biological imaging by soft x-ray diffraction microscopy," *Proc. Natl. Acad. Sci. U.S.A.* 102 (2005) 15343.
- [36] V. Ayvazyan *et al.*, "First operation of a free-electron laser generating GW power radiation at 32 nm wavelength," *Eur. Phys. J. D* 37 (2006) 297.
- [37] K. Tiedtke *et al.*, "The SASE FEL at DESY: Photon Beam Diagnostics for the User Facility, *Proceedings SRI2003*, San Francisco, AIP Conf. Proc. 705 (2004) 588

THE PROPOSED EXPERIMENTAL PROGRAM AT LCLS

I. Lindau, MAX-lab, Lund;
R.W. Falcone, UCB, Berkeley, California

Abstract

I will discuss experiments planned for the LINAC Coherent Light Source, which is under construction at the Stanford Linear Accelerator Center. Experimental Teams have been organized, and construction of a range of instruments is underway. The science program currently includes atomic physics, femtochemistry, nanoscale dynamics in condensed matter physics, structural studies on single particles and biomolecules, and plasma and warm dense matter. New ideas for experiments continue to emerge.

**PAPER NOT
AVAILABLE**